



# Performance of the LHCb Vertex Locator

LHCb VELO Group<sup>†</sup>

## Abstract

The Vertex Locator (VELO) is a silicon microstrip detector that surrounds the proton-proton interaction region in the LHCb experiment. The performance of the detector during the first years of its physics operation is reviewed. The system is operated in vacuum, uses a bi-phase CO<sub>2</sub> cooling system, and the sensors are moved to 7 mm from the LHC beam for physics data taking. The performance and stability of these characteristic features of the detector are described, and details of the material budget are given. The calibration of the timing and the data processing algorithms that are implemented in FPGAs are described. The system performance is fully characterised. The sensors have a signal to noise ratio of approximately 20 and a best hit resolution of 4  $\mu\text{m}$  is achieved at the optimal track angle. The typical detector occupancy for minimum bias events in standard operating conditions in 2011 is around 0.5%, and the detector has less than 1% of faulty strips. The proximity of the detector to the beam means that the inner regions of the  $n^+$ -on- $n$  sensors have undergone space-charge sign inversion due to radiation damage. The VELO performance parameters that drive the experiment's physics sensitivity are also given. The track finding efficiency of the VELO is typically above 98% and the modules have been aligned to a precision of 1  $\mu\text{m}$  for translations in the plane transverse to the beam. A primary vertex resolution of 13  $\mu\text{m}$  in the transverse plane and 71  $\mu\text{m}$  along the beam axis is achieved for vertices with 25 tracks. An impact parameter resolution of less than 35  $\mu\text{m}$  is achieved for particles with transverse momentum greater than 1 GeV/ $c$ .

To be submitted to Journal of Instrumentation

---

<sup>†</sup>Authors are listed on the following page.

## LHCb VELO group

R. Aaij<sup>1</sup>, A. Affolder<sup>2</sup>, K. Akiba<sup>3</sup>, M. Alexander<sup>4</sup>, S. Ali<sup>1</sup>, R.B. Appleby<sup>5</sup>, M. Artuso<sup>6</sup>, A. Bates<sup>4</sup>, A. Bay<sup>7</sup>, O. Behrendt<sup>8</sup>, J. Benton<sup>9</sup>, M. van Beuzekom<sup>1</sup>, P.M. Bjørnstad<sup>5</sup>, G. Bogdanova<sup>10</sup>, S. Borghi<sup>5</sup>, A. Borgia<sup>6</sup>, T.J.V. Bowcock<sup>2</sup>, J. van den Brand<sup>1</sup>, H. Brown<sup>2</sup>, J. Buytaert<sup>8</sup>, O. Callot<sup>11</sup>, J. Carroll<sup>2</sup>, G. Casse<sup>2</sup>, P. Collins<sup>8</sup>, S. De Capua<sup>5</sup>, M. Doets<sup>1</sup>, S. Donleavy<sup>2</sup>, D. Dossett<sup>12</sup>, R. Dumps<sup>8</sup>, D. Eckstein<sup>13</sup>, L. Eklund<sup>4</sup>, C. Farinelli<sup>1</sup>, S. Farry<sup>2</sup>, M. Ferro-Luzzi<sup>8</sup>, R. Frei<sup>7</sup>, J. Garofoli<sup>6</sup>, M. Gersabeck<sup>5</sup>, T. Gershon<sup>12</sup>, A. Gong<sup>14</sup>, H. Gong<sup>14</sup>, H. Gordon<sup>8</sup>, G. Haefeli<sup>7</sup>, J. Harrison<sup>5</sup>, V. Heijne<sup>1</sup>, K. Hennessy<sup>2</sup>, W. Hulsbergen<sup>1</sup>, T. Huse<sup>15</sup>, D. Hutchcroft<sup>2</sup>, A. Jaeger<sup>16</sup>, P. Jalocha<sup>17</sup>, E. Jans<sup>1</sup>, M. John<sup>17</sup>, J. Keaveney<sup>18</sup>, T. Ketel<sup>1</sup>, M. Korolev<sup>10</sup>, M. Kraan<sup>1</sup>, T. Laštovička<sup>19</sup>, G. Lafferty<sup>5</sup>, T. Latham<sup>12</sup>, G. Lefevre<sup>6</sup>, A. Leflat<sup>10</sup>, M. Liles<sup>2</sup>, A. van Lysebetten<sup>1</sup>, G. MacGregor<sup>5</sup>, F. Marinho<sup>20</sup>, R. McNulty<sup>21</sup>, M. Merkin<sup>10</sup>, D. Moran<sup>22</sup>, R. Mountain<sup>6</sup>, I. Mous<sup>1</sup>, J. Mylroie-Smith<sup>2</sup>, M. Needham<sup>23</sup>, N. Nikitin<sup>10</sup>, A. Noor<sup>2</sup>, A. Oblakowska-Mucha<sup>24</sup>, A. Papadelis<sup>1</sup>, M. Pappagallo<sup>4</sup>, C. Parkes<sup>5</sup>, G.D. Patel<sup>2</sup>, B. Rakotomiaramanana<sup>7</sup>, S. Redford<sup>8</sup>, M. Reid<sup>12</sup>, K. Rinnert<sup>2</sup>, E. Rodrigues<sup>5</sup>, A.F. Saavedra<sup>25</sup>, M. Schiller<sup>1</sup>, O. Schneider<sup>7</sup>, T. Shears<sup>2</sup>, R. Silva Coutinho<sup>12</sup>, N.A. Smith<sup>2</sup>, T. Szumlak<sup>24</sup>, C. Thomas<sup>17</sup>, J. van Tilburg<sup>1</sup>, M. Tobin<sup>7</sup>, J. Velthuis<sup>9</sup>, B. Verlaat<sup>1</sup>, S. Viret<sup>26</sup>, V. Volkov<sup>10</sup>, C. Wallace<sup>12</sup>, J. Wang<sup>6</sup>, A. Webber<sup>5</sup>, M. Whitehead<sup>12</sup>, E. Zverev<sup>10</sup>.

<sup>1</sup>*Nikhef National Institute for Subatomic Physics, Amsterdam, Netherlands*

<sup>2</sup>*Oliver Lodge Laboratory, University of Liverpool, Liverpool, United Kingdom*

<sup>3</sup>*Universidade Federal do Rio de Janeiro (UFRJ), Rio de Janeiro, Brazil*

<sup>4</sup>*School of Physics and Astronomy, University of Glasgow, Glasgow, United Kingdom*

<sup>5</sup>*School of Physics and Astronomy, University of Manchester, Manchester, United Kingdom*

<sup>6</sup>*Syracuse University, Syracuse, NY, United States*

<sup>7</sup>*Ecole Polytechnique Fédérale de Lausanne (EPFL), Lausanne, Switzerland*

<sup>8</sup>*European Organization for Nuclear Research (CERN), Geneva, Switzerland*

<sup>9</sup>*H.H. Wills Physics Laboratory, University of Bristol, Bristol, United Kingdom*

<sup>10</sup>*Institute of Nuclear Physics, Moscow State University (SINP MSU), Moscow, Russia*

<sup>11</sup>*LAL, Université Paris-Sud, CNRS/IN2P3, Orsay, France*

<sup>12</sup>*Department of Physics, University of Warwick, Coventry, United Kingdom*

<sup>13</sup>*Deutsches Elektronen-Synchrotron, Hamburg, Germany*

<sup>14</sup>*Center for High Energy Physics, Tsinghua University, Beijing, China*

<sup>15</sup>*Department of Physics, University of Oslo, Oslo, Norway*

<sup>16</sup>*Physikalisches Institut, Ruprecht-Karls-Universität Heidelberg, Heidelberg, Germany*

<sup>17</sup>*Department of Physics, University of Oxford, Oxford, United Kingdom*

<sup>18</sup>*Vrije Universiteit Brussel, Brussel, Belgium*

<sup>19</sup>*Institute of Physics, Academy of Sciences of the Czech Republic, Prague, Czech Republic*

<sup>20</sup>*Universidade Federal do Rio de Janeiro, Campus UFRJ - Macaé, Rio de Janeiro, Brazil*

<sup>21</sup>*School of Physics, University College Dublin, Dublin, Ireland*

<sup>22</sup>*Universidad Autónoma de Madrid, Spain*

<sup>23</sup>*School of Physics and Astronomy, University of Edinburgh, Edinburgh, United Kingdom*

<sup>24</sup>*AGH - University of Science and Technology, Faculty of Physics and Applied Computer Science, Kraków, Poland*

<sup>25</sup>*School of Physics, University of Sydney, Sydney, Australia*

<sup>26</sup>*Université de Lyon, Université Claude Bernard Lyon 1, CNRS-IN2P3, Institut de Physique Nucléaire de Lyon, Villeurbanne, France*

# Contents

<b>1</b>	<b>Introduction</b>	<b>1</b>
<b>2</b>	<b>Subsystem performance</b>	<b>5</b>
2.1	Commissioning results . . . . .	5
2.2	Vacuum stability . . . . .	6
2.3	Cooling performance . . . . .	7
2.4	Low voltage and high voltage . . . . .	8
2.5	Motion performance . . . . .	9
2.6	Material description . . . . .	10
<b>3</b>	<b>Calibration, monitoring and simulation</b>	<b>14</b>
3.1	Data acquisition system . . . . .	14
3.2	Timing and gain . . . . .	14
3.2.1	ADC sampling time . . . . .	15
3.2.2	Gain . . . . .	15
3.2.3	Timing to the beam . . . . .	16
3.3	FPGA data processing algorithms . . . . .	17
3.3.1	Pedestal subtraction . . . . .	19
3.3.2	Mean common mode suppression . . . . .	19
3.3.3	Topological strip channel reordering . . . . .	21
3.3.4	Zero suppression and clusterisation . . . . .	22
3.4	Error identification . . . . .	22
3.4.1	Single event upsets . . . . .	23
3.5	Monitoring . . . . .	23
3.6	Simulation . . . . .	25
<b>4</b>	<b>Overall system performance</b>	<b>26</b>
4.1	Signal size and noise rate . . . . .	26
4.2	Resolution . . . . .	27
4.3	Occupancy . . . . .	30
4.4	Beam backgrounds and high multiplicity events . . . . .	32
4.5	Efficiency and faulty channel analysis . . . . .	33
4.6	Radiation damage studies . . . . .	36
4.6.1	Current measurements . . . . .	36
4.6.2	Effective doping concentration . . . . .	37
4.6.3	Charge loss to second metal layer . . . . .	38
<b>5</b>	<b>Physics performance</b>	<b>40</b>
5.1	Pattern recognition and tracking . . . . .	40
5.2	Alignment . . . . .	42
5.2.1	Optical and mechanical measurements . . . . .	43
5.2.2	Track-based alignment methods . . . . .	43

5.2.3	Mechanical measurement of closing . . . . .	44
5.2.4	Alignment performance . . . . .	44
5.3	Primary vertex resolution . . . . .	46
5.4	Impact parameter resolution . . . . .	47
5.5	Decay time resolution . . . . .	50
<b>6</b>	<b>Conclusions</b>	<b>53</b>
<b>7</b>	<b>Acknowledgements</b>	<b>54</b>
	<b>References</b>	<b>55</b>

# 1 Introduction

LHCb [1] is an experiment dedicated to heavy flavour physics at the LHC. Its primary aim is to discover new physics through precision studies of CP violation and rare decays of beauty and charm hadrons. The detector is comprised of the Vertex Locator (VELO), silicon strip and straw chamber trackers, a warm dipole magnet, ring imaging Cherenkov particle identification systems, calorimeters and a muon detection system.

The LHCb Vertex Locator [2] is a silicon microstrip detector positioned around the proton-proton interaction region. The VELO provides measurements of track coordinates which are used to identify the primary interaction vertices and the secondary vertices that are a distinctive feature of  $b$ - and  $c$ -hadron decays. The VELO was designed to optimise the LHCb physics programme in the following ways:

- **Angular coverage.** The VELO is designed to cover the forward region, such that all tracks inside the nominal LHCb acceptance of 15–300 mrad cross at least three VELO stations. In this way the detector fully reconstructs roughly 27% of  $b\bar{b}$  production for 7 TeV proton-proton centre-of-mass collisions, while covering just 1.8% of the solid angle [3, 4]. The VELO also reconstructs tracks in the forward direction and backward directions which do not have momentum information, but are useful to improve the primary vertex reconstruction.
- **Triggering.** The reconstruction of the primary vertex and the displaced secondary decay vertex of a heavy flavour hadron in the VELO is a key ingredient of the high level trigger which reduces the event rate from a 1 MHz event rate to a few kHz [5].
- **Efficient reconstruction.** LHCb has studied decay modes with up to six charged tracks in the final state [6]. This relies on the highly efficient cluster reconstruction in the VELO since track reconstruction efficiency losses are transmitted as the sixth power. The cluster reconstruction efficiency in the VELO is paramount, both for the selection of those tracks, as six measurements per track are required, and for efficient pattern recognition and fake track rejection.
- **Displaced tracks and vertices.** Excellent vertex resolution is essential to the LHCb physics programme. Most analyses rely heavily on selection cuts on the distance with which tracks approach the primary vertex (impact parameter) and on the displaced vertex reconstruction with the VELO to identify the signal channels. The impact parameter resolution was optimised by positioning the VELO sensors as close to the LHC beam as permitted by safety consideration, having a small inter-strip pitch at the inside of the sensors, and minimising the amount of material traversed by a particle before the first measured hits in the VELO.
- **Decay time.** The decay time of a particle is obtained from the measurement of its flight distance in the VELO. This is required for lifetime measurements and, critically, for time-dependent measurements in the rapidly oscillating  $B_s^0-\bar{B}_s^0$  meson system [7, 8].

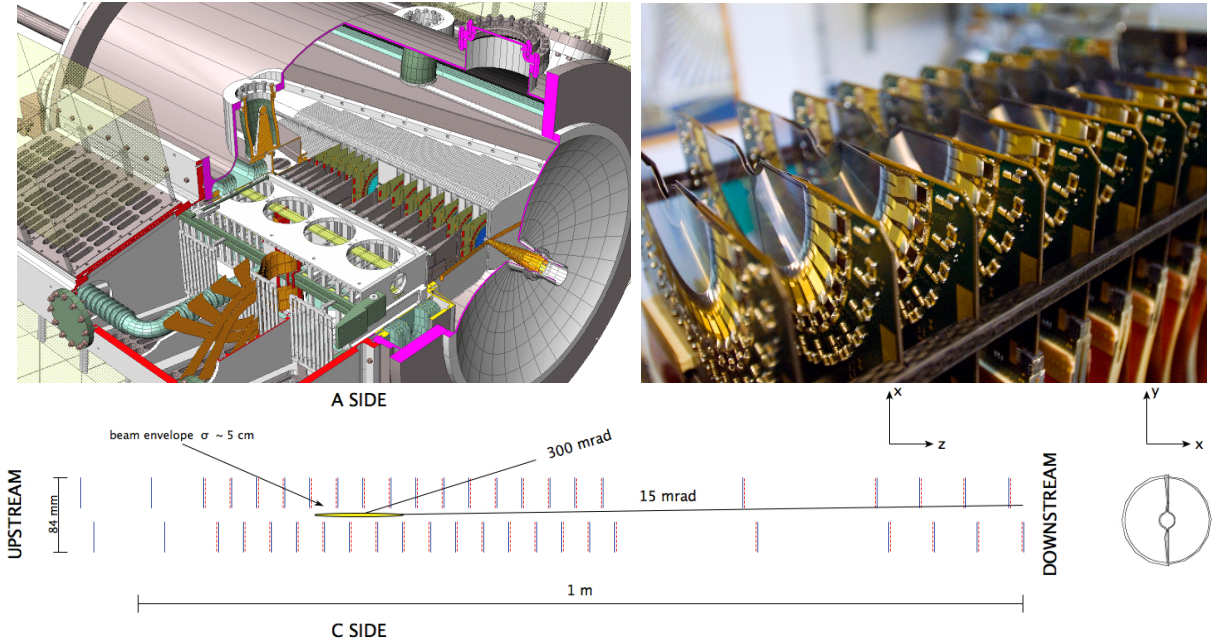


Figure 1: (top left) The LHCb VELO vacuum tank. The cut-away view allows the VELO sensors, hybrids and module support on the left-hand side to be seen. (top right) A photograph of one side of the VELO during assembly showing the silicon sensors and readout hybrids. (bottom) Cross-section in the  $xz$  plane at  $y = 0$  of the sensors and a view of the sensors in the  $xy$  plane. The detector is shown in its closed position.  $R$  ( $\Phi$ ) sensors are shown with solid blue (dashed red) lines. The modules at positive (negative)  $x$  are known as the left or A-side (right or C-side).

The VELO contains a series of silicon modules arranged along the beam direction, see Fig. 1. A right-handed co-ordinate system is defined with  $z$  along the beam-axis into the detector,  $y$  vertical and  $x$  horizontal. Cylindrical polar co-ordinates  $(r, \theta, \phi)$  are also used. The region of the detector at positive (negative)  $z$  values is known as the forward (backward) or downstream (upstream) end.

The sensors are positioned only 7 mm from the LHC beams. This is smaller than the aperture required by the LHC beam during injection. Hence, the detector is produced in two retractable halves. There is a small overlap between the two detector halves when closed. This aids alignment and ensures that full angular coverage is maintained. The position of the VELO halves are moveable in  $x$  and  $y$  and the VELO is closed at the beginning of each fill such that it is centred on the interaction region.

Approximately semi-circular silicon sensors are used. Each module contains one  $r$  and one  $\phi$  coordinate measuring sensor, known as  $R$  and  $\Phi$  sensors and shown schematically in Fig. 2. The inter-strip pitch varies from approximately 40 to 100  $\mu\text{m}$  across the sensor. The strips are read out from around the circumference of the sensor through the use of routing lines on the sensor. The sensors are read out using the Beetle [9] analogue front-end ASIC, operated with a 40 MHz input event sampling rate. The signals are digitised and processed

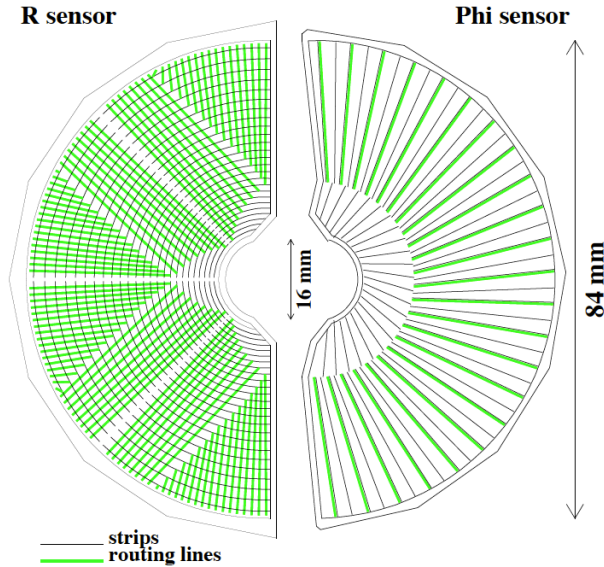


Figure 2: Schematic representation of an  $R$  and a  $\Phi$  sensor. The  $R$  sensor strips are arranged into four approximately  $45^\circ$  segments and have routing lines perpendicular to the strips. The  $\Phi$  sensor has two zones with inner and outer strips. The routing lines of the inner strips are orientated parallel to the outer strips.

to form clusters in an FPGA-based readout board known as the TELL1 [10], before being passed to the high level trigger. More details on the readout chain are given in Sect. 3.1

There are 21 standard modules in each VELO half. Two further modules, known as the pile-up system, containing  $R$  sensors only are located in the most upstream positions.

Owing to the proximity of the detector to the beam, the VELO is exposed to a high radiation fluence and radiation tolerant oxygenated  $n^+$ -on- $n$  sensors, consisting of an  $n$ -type implant on an  $n$ -type bulk with a backplane  $p^+$ -type implant, are employed. One of the most upstream modules uses  $n^+$ -on- $p$  silicon (one  $R$  and one  $\Phi$  sensor pair). These are the only  $n^+$ -on- $p$  sensors in operation at the LHC and were installed as this technology is a leading candidate for use in the LHC upgrades. All sensors were fabricated by Micron Semiconductor.<sup>1</sup>

The detectors are mounted in a vacuum vessel and are located in a secondary vacuum separated from the LHC machine vacuum by an RF-box. The surfaces facing the beam are 0.3 mm thick corrugated sheets, known as the RF foil. These RF-boxes and foil provide three functions: they provide shielding against RF pickup from the LHC beams, guide wakefields to prevent impedance disruptions to the LHC beams, and protect the LHC vacuum from outgassing of the detector modules. The detector is located upstream of the LHCb dipole magnet in a region with a negligible magnetic field.

<sup>1</sup>Micron Semiconductor Ltd., 1 Royal Buildings, Marlborough Road, Lancing Business Park, Lancing, Sussex, BN15 8SJ, UK.

This paper reports on the performance of the VELO detector over the first period of LHC physics operation. The first proton-proton collisions occurred in November 2009 at beam energies of 450 GeV, with the first 3.5 TeV beam collisions occurring in March 2010. The beam energy was raised further to 4 TeV in April 2012. All physics data were recorded with a 50 ns minimum bunch spacing. LHCb recorded integrated luminosities of  $0.04 \text{ fb}^{-1}$  in 2010,  $1.11 \text{ fb}^{-1}$  in 2011 and  $2.08 \text{ fb}^{-1}$  in 2012. The first period of LHC operations ended in February 2013, when the LHC entered a shutdown for an upgrade to increase the beam energy. The LHCb VELO performance results in this paper are primarily given on 2011 data, the first year in which the instantaneous luminosity reached, and exceeded, the nominal design value. Section 2 describes the performance of the component subsystems in the VELO. The calibration of the timing, gain and processing parameters is described in Sect. 3, along with the detector monitoring strategy and the simulation and reconstruction software. Sections 4 and 5 provide the system performance results, with the former section providing detector performance related results and the latter results on quantities more directly related to physics performance.



## 2 Subsystem performance

The performance of individual subsystems from the VELO are described in this section. The section starts with a description of the commissioning stages of the detector and then describes the performance of the vacuum, cooling, low and high voltage and motion systems. The section ends with information on the material budget of the VELO.

### 2.1 Commissioning results

The subsystems and overall operations of the VELO were extensively commissioned before the first LHC beam collisions. After production, the commissioning of the VELO consisted of four main stages: testing during assembly, operation in a test beam, commissioning post-installation at the LHCb experimental area, and testing with beam-absorber collisions.

The detectors underwent extensive quality assurance tests at the production sites and after delivery for system assembly, utilising components of the final readout system [11]. During detector assembly (Fig. 1 shows a photograph of the system at this stage) each module was operated with a complete readout slice, simulating as closely as possible the final vacuum, cooling, and powering conditions of the VELO. The main mechanical difference from the final system was the absence of the RF foil. This first testing step allowed a complete “fingerprint” of the pedestal and noise map of each module to be produced, along with the commissioning of the zero suppression algorithms running in the TELL1 DAQ boards (see Sect. 3.3).

In the second step, a partially assembled VELO half was taken to the 120 GeV pion/muon beam at the North area SPS test beam facility at CERN. Complete track and vertex reconstruction was performed, using the products of interactions of the beam in lead targets placed in similar positions to that of the LHC beam interaction region [12]. This allowed the data acquisition and software chain to be debugged, in addition to performing a full speed test of significant components of the LHCb readout chain. It also served as a “dress rehearsal” for the transportation of the VELO using a truck with special traction and speed control. The VELO half was mounted on four shock absorbers on a trailer with special suspension, and the transport motion was fully logged using accelerometers.

The third stage of the commissioning was carried out after the installation of the VELO at the LHCb experimental area. Due to the proximity of the silicon sensors ( $\leq 1$  mm) to the 1 m long corrugated RF foil, and the insertion procedure of the detector halves into the RF foil relying purely on the manufacturing and assembly tolerances, it was necessary to employ special monitoring procedures. Each module slot was tested with an oversized dummy sensor model for contact with the foil, and a test insertion was performed with a genuine module. Characteristic IV curves of all sensors were taken at several occasions during the transport, movement and installation procedures, and it was verified that no damage had occurred. Following this, the cabling of the detector was verified by applying custom test-pulse patterns to each of the 5632 readout links, and verifying the correct pattern was read back. Each link was tuned to select the optimal ADC sampling point using test-pulses (see Sect. 3.2.1). The digitisation uniformity was confirmed by

injecting sine wave pulses with an amplitude close to the full dynamic range and a period matching the pulse train from the front-end ASICs. In addition, the noise and pedestals were measured, and compared with the “fingerprint” recorded during the assembly and commissioning process.

In the fourth and final commissioning step, a special method was found to study genuine tracks in the detector before the start of LHC collisions. The synchronisation tests of the LHC beam were utilised in which, during the initial phase of each test, the LHC proton beam was collided with a beam absorber at the end of the transfer line between the CERN SPS and the LHC about 340 m from the LHCb cavern. This allowed the VELO to reconstruct the first tracks from the LHC machine [13]. The particles produced by the proton interactions in the absorber, and by their re-interaction, were detected by the LHCb experiment and were used to commission the detector. These injection tests were performed in 2008 before the first circulating beam in the LHC and in 2009 before the first proton-proton collisions. These data were used to set up the timing and the alignment of the system, and for commissioning of the control, reconstruction and monitoring software. They were of particular importance to the VELO as it is not possible to collect sufficient cosmic ray data for commissioning due to the horizontal geometry, and hence provided the first full system test of the VELO. With this method about 50k tracks were reconstructed in LHCb. This was sufficient to determine that the modules were displaced by less than 10  $\mu\text{m}$  from their surveyed positions (see Sect. 5.2). The alignment of the modules was determined with 5  $\mu\text{m}$  precision for  $x$  and  $y$  translation and 200  $\mu\text{rad}$  for the rotations around the  $z$ -axis [14]. In addition, the tracks traversing from one VELO half to the other could be used, by evaluating the mismatch of the two segments, to measure the distance between the halves to a precision of 100  $\mu\text{m}$ . The time alignment of the VELO was determined to a precision of 2 ns, and measurements made of the signal to noise and cluster finding efficiency. These commissioning stages allowed LHCb to be ready for an immediately successful start to physics data taking after the first LHC beams collided in November 2009.

## 2.2 Vacuum stability

The VELO vacuum vessel is composed of two sections: the first is part of the beam volume of the LHC, and the other contains the detector modules. The two sections are separated by a vacuum tight RF-box, welded from a 0.3 mm thick corrugated AlMg3 foil with 0.5 mm thick side walls which encapsulates each detector half. The differential pressure between the beam and detector volume should always remain below 5 mbar to protect the foil against irreversible deformation. Consequently, the pump-down and gas venting procedures are very delicate operations that are controlled by a programmable logic controller (PLC), based on the readings from three membrane switches that have preset trigger values. The PLC continuously monitors the performance of the system and takes, when needed, appropriate actions. A PVSS<sup>2</sup> project monitors and archives all relevant system variables

---

<sup>2</sup>PVSS is a Supervisory Control and Data Acquisition software package developed by ETM professional control GmbH.

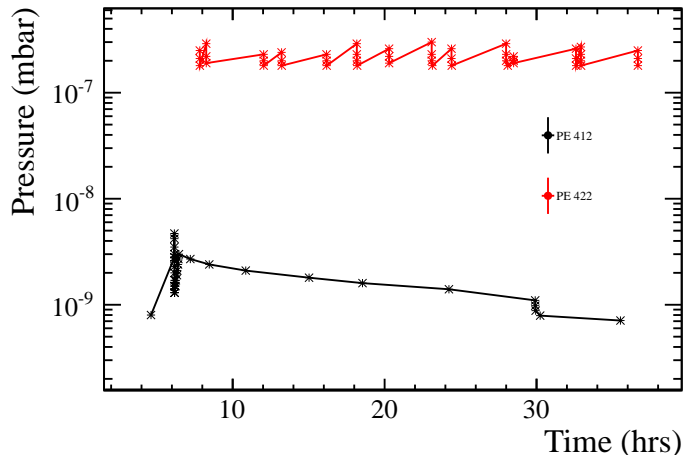


Figure 3: Illustration of the influence of the proton beams on the beam volume pressure. The readings of the beam volume (PE 412) and detector volume (PE 422) are shown, and the increase in pressure in the beam volume coinciding with the beam injections (each containing  $2 \times 10^{14}$  protons) at  $t = 6$  hours can be seen. The beams were dumped 24 hours later.

in a database, that is common to the whole LHCb experiment [15]. For redundancy purposes, two sets of roughing, turbo-molecular and ion pumps are implemented in the system. The pressure in the detector volume is around  $2 \times 10^{-7}$  mbar, while the beam volume is at  $1 \times 10^{-9}$  mbar in the absence of circulating beams. Under the influence of 1380 bunches per beam this pressure can rise to  $5 \times 10^{-9}$  mbar. The influence of the proton beams on the pressure of the beam volume can clearly be seen in Fig. 3.

### 2.3 Cooling performance

The VELO modules are cooled by means of an evaporative system using  $\text{CO}_2$  as coolant. The cooling plant, which is located outside the radiation zone, has two chillers filled with hydrofluorocarbon (R507a): a 2.5 kW water-cooled main chiller and a 1 kW air-cooled backup chiller, operating at  $-40$  and  $-25^\circ\text{C}$ , respectively (see Ref. [16]). The actual cooling system of the detector consists of two parallel, largely independent, loops: one for each detector half. The  $\text{CO}_2$  is subcooled by the main chiller and subsequently pumped to the corresponding detector via a 55 m long transfer line. The operation principle is that of a bi-phase accumulator controlled loop, in which the evaporative temperature in the detector is regulated by controlling the pressure of the saturated mixture of vapour and liquid in the accumulator. The cooling system is controlled by a PLC. In total 31 pressure and 192 temperature sensors are installed throughout the system. The PLC controls the system via 24 proportional, integrating and differentiating loops based on a subset of these readings. Alarm handling tasks are executed continuously and if appropriate the system switches to the backup chiller or a spare pump. A PVSS project monitors and archives

all relevant system variables in an Oracle database that is common to the whole LHCb experiment. A separate heating system takes care of maintaining the temperature of the module base at 20°C to minimise deformations.

The default evaporator temperature is  $-28^{\circ}\text{C}$ . Due to thermal gradients between the cooling blocks and the components of the hybrid the silicon temperatures are  $(-7 \pm 2)^{\circ}\text{C}$ . From the moment the front-end electronics is switched on, it takes 3 minutes till the hybrid temperatures have stabilised. The hybrid temperatures have been shown to be stable within  $0.1^{\circ}\text{C}$  over a period of four weeks.

The operation of the cooling system has been very smooth. The only major intervention required was the replacement of the insulation of the transfer lines in 2011 to eliminate the formation of ice. During operations in both 2009 and 2011 an increase of  $\sim 1^{\circ}\text{C}$  was observed in one detector half and found to be due to clogging of filters: the filters were replaced during the following winter shutdowns.

During injection and ramp of the beams, the temperatures of the RF-boxes increase by  $0.5^{\circ}\text{C}$ . Subsequently the temperatures of the RF-boxes decrease by  $1.5^{\circ}\text{C}$  when the VELO is closed.

## 2.4 Low voltage and high voltage

Each silicon sensor has its own hybrid with separate low voltage (LV) and high voltage (HV) supplies. In addition, repeater boards are located directly outside the VELO vacuum tank, which have their own positive and negative supplies. Both the LV and HV power supplies are inside the counting-house shielded from the radiation zone of the detector.

The LV system is based on the A3009 EASY low voltage module, with compatible crates and mainframe controller, manufactured by CAEN.<sup>3</sup> The main system performance issue has been with the LV Anderson connectors used in the system. Due to oxidation a voltage drop across the connector can occur. This requires careful monitoring as the dissipated power caused severe thermal damage on one of the connectors during operation. The connectors were replaced by CAEN during the shutdown at the end of 2011.

The HV system is based on the EHQ F607n-F 16-channel HV module from Iseg.<sup>4</sup> Careful monitoring of the HV parameters is a key requirement as the current and depletion voltage change with radiation damage (see Sect. 4.6). The main performance issue was with the control of the HV supplies. The supplies occasionally get stuck when ramping in voltage, requiring the software commands to be resent or control software restarted.

Voltage and current monitoring are implemented for both LV and HV systems and they are connected to an FPGA based interlock safety system. All HV and LV modules can have their channels switched off quickly ( $< 1$  s) by the interlock system in case of problems. The primary uses of the interlock system have been in the case of power cuts or disruptions, and interruptions to the chilled water supply that is used by the cooling system.

---

<sup>3</sup>CAEN S.p.A., Via Vetraria 11, 55049 - Viareggio (LU) - Italy.

<sup>4</sup>Iseg Spezialelektronik GmbH, Bautzner Landstr. 23, 01454 Radeberg / OT Rossendorf, Germany.

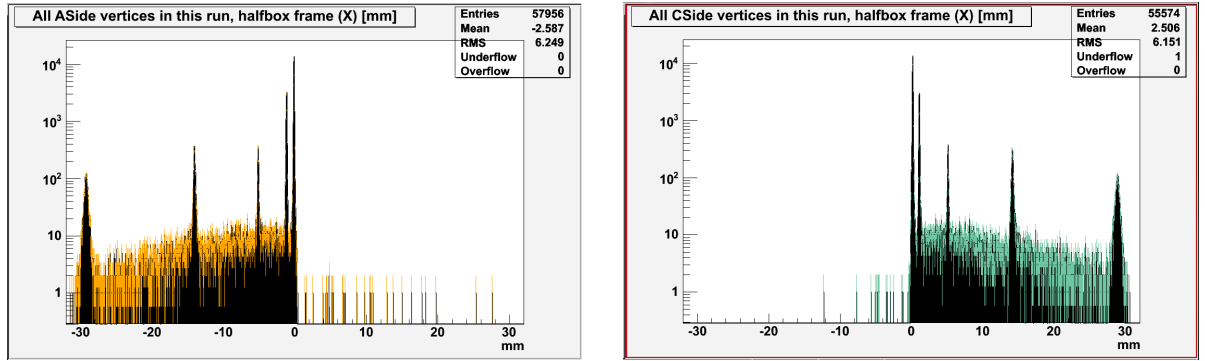


Figure 4: The horizontal position of LHC collision vertices as reconstructed by the A-Side (left) and C-Side (right). These online screenshots of data illustrate the “stop-measure-move” cycle of the closing procedure, where each peak in the distribution corresponds to a “stop”, as well as the degradation of vertex resolution with opening distance.

## 2.5 Motion performance

The first active silicon strips are brought to within 8.2 mm of the LHC beams, with the inner surface of the RF foil at a 5.5 mm radius. To ensure detector safety during beam injection and adjustments, each VELO half is retracted  $\sim 29$  mm in the horizontal plane and is only closed once stable-beam conditions are declared. The VELO halves are moved using radiation hard stepper motors, and the motion towards the final position is always done from the same direction in order to minimise the effects of mechanical backlash. The position is read from resolvers mounted on the motor axes. The reproducibility of the position has been measured to be better than  $10 \mu\text{m}$ . The motion system is controlled by a PLC which performs many safety checks to prevent unwanted movements due to hardware failures or corruption of the destination position calculated by the closing procedure.

An automated closure procedure has been developed to position the VELO halves around the beams, whilst taking into account the current beam conditions. It uses information about the background level, the response of the hardware and the positions of the beams to make informed decisions. During closure, the LHCb trigger accepts 500 Hz of events which are required to contain at least one track in the VELO. This rate ensures that a new beam-position measurement, consisting of 400 reconstructed vertices, can be acquired in 1–2 s, even in the most open position. Figure 4 shows an example of the distribution of vertices during a typical closure.

Upon receiving notification of stable beams, the two VELO halves are moved in a series of “stop-measure-move” steps from open to closed. A vertical adjustment is also made at each of the steps, if the movement required to centre the VELO around the beams is greater than  $20 \mu\text{m}$ . Three criteria are checked at all times during and after closure:

1. the total silicon bias current from the 44 sensors in each half of the VELO is less than  $1000 \mu\text{A}$  above the dark current. This limit corresponds to 10% occupancy of ionising particles in all sensors for several seconds;

2. the Beam Conditions Monitors [17] — each consisting of eight CVD-diamond radiation monitors placed adjacent to the beam pipe — are all functional and reporting fluences less than 5% of the threshold which triggers an LHC beam dump;
3. the reconstructed beam position in  $x$  and  $y$ , as measured by the two halves, agree given the known opening distance at any given step. The observed beam width must be acceptable given the opening distance and the expected resolution thereof.

By considering the two independent beam profiles compiled by each half, the VELO is observed to close symmetrically to an accuracy of better than  $4\ \mu\text{m}$ .

Once closed the monitoring continues throughout the data taking. Apart from requiring the above conditions, a slow drift of the beams is protected against by prompting the VELO to open if the beams move by more than  $300\ \mu\text{m}$ . The LHC beam orbit has shown excellent stability. Consequently, the VELO is permitted to remain closed for up to 20 minutes if the reconstruction of the beam profiles is interrupted. This happens, for example, if the LHCb data acquisition is paused (e.g. for a run change or reconfiguration). During this grace period, movement of the beam is monitored by the LHC beam position monitors which are horizontal and vertical wire pickups located at  $z = \pm 22\ \text{m}$  of the collision region. A deviation of  $200\ \mu\text{m}$  in any of these readings will trigger the VELO to open.

The initial use of the system was performed with careful manual checking and control of the closings. The automated closing procedure was then put in place. From the declaration of stable beams the VELO takes, on average, 210 s to close. Of this 160 seconds is due to the motion from the open to closed positions. During the operations in 2010–2012 approximately 750 closing procedures were performed and 0.9% of the stable-beam integrated luminosity delivered by the LHC was lost due to this detector-safety procedure. This number is in line with the expectation. Only minor performance problems have been encountered and these have been addressed with changes to the closing procedure, safety checks and motion PLC code.

## 2.6 Material description

The minimisation of the material budget of the detector is important for the physics performance of the experiment in order to reduce the amount of multiple scattering and particle interactions with material. An accurate description of the material is also required for the simulation of the experiment and for estimating the amount of multiple scattering that particles undergo when performing track reconstruction. The material description is implemented using the basic volumes in GEANT4 [18] and there are limits on the accuracy that is achievable, both from the range of basic volumes (and combinations thereof) that are available and from the CPU time taken to process very complex composite volumes. The appropriate balance must therefore be obtained between accuracy and simplicity for each element of the description. This is particularly an issue for the description of the complex RF foil shape (see Fig. 6 below).

A comparison has been made between the measured masses of the various elements of the detector, as determined at production, and their simulated counterparts, which in

general shows very good agreement, *e.g.* the average mass of the sensors is  $(2.17 \pm 0.03)$  g, compared with the simulated mass of 2.14 g. Similarly the mass of the dominant component of the material, the RF foil, is reproduced to within 2%. The RF foil was manufactured as a single sheet of aluminium magnesium alloy and then pressed into its rather complex shape. So while the agreement of the total material may be good, the distribution of that material might not be so well described. Tests were performed by measuring the thickness of an RF foil and it was found that the amount of material was too low in regions around the beam in the description used up till 2012 and this has now been improved. While this has only a small effect on the total material it does contribute significantly to the material before the first measured point, which is important for the impact parameter performance with lower momentum tracks (see Sect. 5.4).

The simulated detector description can be used to estimate the material traversed by a particle as it moves through the VELO. Figure 5 (left) shows the amount of material along the trajectory of a particle, which originates from the interaction point, before it reaches the radius of the first active strip on the detector (8.2 mm), as a function of pseudorapidity and azimuthal angle. The amount of material is expressed in terms of the fraction of a radiation length ( $X_0$ ) and the average material in the VELO acceptance passed through before reaching this radius is  $0.042 X_0$ . The average amount of material traversed before a particle leaves the VELO at  $z = 835$  mm is  $0.227 X_0$ . The breakdown of this total material budget into the components of the VELO system inside the acceptance is shown in Fig. 5 (right). The VELO design means that much of the electronics and services are outside the detector acceptance. The RF foil dominates with  $\sim 43\%$  of the material, and the next largest component is the active silicon sensors. Considering the uncertainty on all components of the VELO, the material traversed by a typical particle is estimated as being known to an accuracy of  $\pm 6\%$ .

A particle traversing the VELO can interact with the material, potentially producing a number of other particles in the interaction. If some or all of these particles are charged and their trajectories are within the VELO acceptance they can be tracked and the vertex of the interaction reconstructed. By examining the density distribution of these reconstructed vertices the material distribution can be studied. The procedure is applied to a sample of data arising from interactions of the beam with gas molecules in the beam pipe as this provides a more uniformly distributed flux of interactions than in collision events.

Figure 6 shows the distribution of vertices in a cross-section of the VELO between  $y = -5$  mm and  $y = +5$  mm. The vertices are plotted in the  $r'z$  plane, where  $r'$  is the radial distance from the beam axis of the vertex multiplied by either 1 or  $-1$  depending on the sign of the  $x$  coordinate to separate the left and right halves of the detector. Vertices with a radius less than 5 mm are not plotted. The top right and bottom left components of the figure focus on a more restricted region in  $z$ , just downstream of the interaction point in data and simulation. The main features of the  $R$  and  $\Phi$  sensors in each module and the undulating form of the RF foil can clearly be seen. The most striking difference between data and simulation is the more angular form of the simulated RF foil.

Another useful feature of these vertex distributions is that they allow checks to be performed of the relative positions of the various VELO components. The proximity of

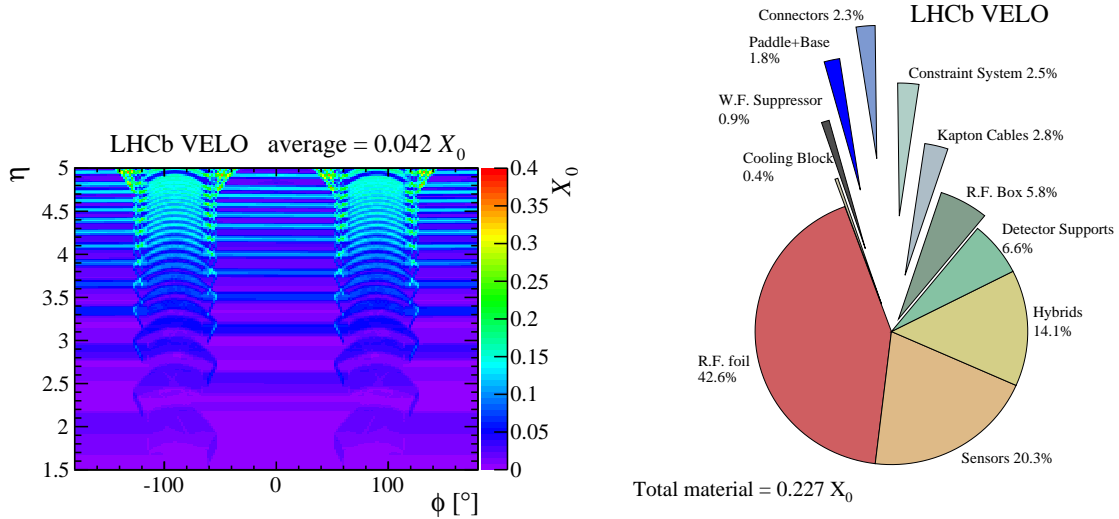


Figure 5: (left) Material passed through on trajectories originating from the interaction point and terminating at the radius of the first active strip in the detector expressed in terms of the fraction of a radiation length ( $X_0$ ) and as a function of pseudorapidity ( $\eta$ ) and azimuthal angle ( $\phi$ ). The material is higher in the regions around  $\pm 90^\circ$  where the two halves of the detector overlap. (right) Breakdown of the total material budget by component of the VELO. The number given for each component is the percentage of the total average VELO material budget ( $0.227 X_0$ ).

the sensors to the RF foil is of particular interest since if these were to touch it could lead to an electrical short or damage to the RF foil. Figure 6 (bottom right) shows the material interactions in the region around one of the pile-up veto stations which have a single sensor. It is clear that in this pile-up station the sensor is quite close to, though not actually touching, the foil. All of the VELO stations have a greater clearance from the foil.

These data can also be used to make a determination of the aperture available to the beam due to the mechanical tolerances of the RF foil construction and positioning. This information is of particular interest for the upgrade of the VELO in which the radius of the detector, and hence of the RF foil, is to be reduced [19]. The vertices attributed to interactions in the RF foil in the  $z$  regions around the sensors where the foil is at its smallest radius are selected. Information can be obtained on the available beam aperture by fitting the data with a circle and extracting the variations [20]. Conservatively assuming a foil thickness of  $300 \mu\text{m}$ , an aperture of  $4.9 \text{ mm}$  is obtained, to be compared with the nominal value of  $5.5 \text{ mm}$ . This is further reduced to  $4.5 \text{ mm}$  by the weld of the foil to the RF box but is still well within the tolerance of  $2.4 \text{ mm}$  that was reserved for mechanical imperfections of the foil with regard to the beam aperture.



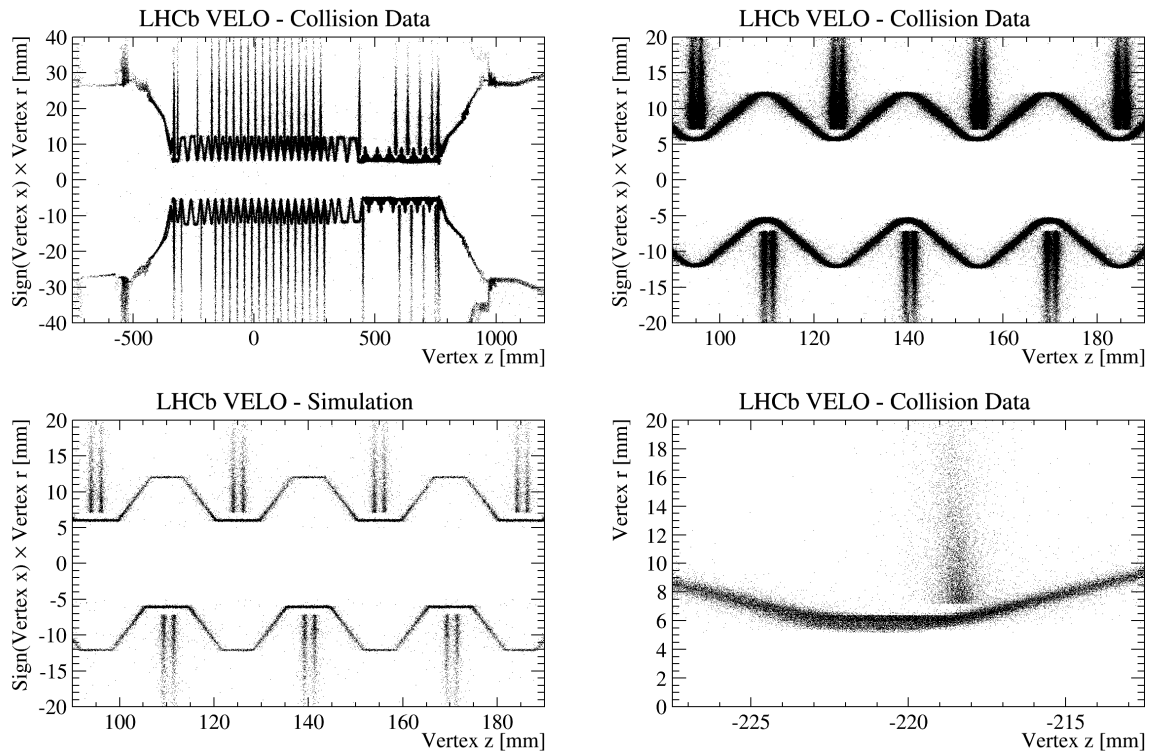


Figure 6: Vertices of hadronic interactions in the LHCb VELO material. (top left) Full VELO system with entrance and exit regions visible in data. (top right) Zoom in to a group of sensors downstream from the interaction point in data. (bottom left) the same region reconstructed using simulation events. (bottom right) Zoom onto an pile-up module consisting of a single R-sensor to check the distance between the sensor and foil.

## 3 Calibration, monitoring and simulation

The performance of the VELO depends critically on its calibration. This section describes the calibration of the timing and gain of the detector, and the data processing algorithms that are executed in FPGAs. The determination and verification of the parameters of these algorithms are discussed. The section starts with a brief description of the data acquisition system (DAQ). The simulation of the detector is also described at the end of the section.

### 3.1 Data acquisition system

The silicon sensor's strips are connected to the Beetle front-end ASICs [9] on the hybrid circuit boards of the VELO modules. The ASIC samples data with the LHC bunch crossing frequency and stores them in an analogue pipeline, with a length of 160 events, awaiting the decision of the first level trigger. Both the shape of the Beetle front-end amplifier pulse response and the sampling time can be tuned in order to get the best performance; the tuning procedure for the sampling time is described in Sect. 3.2.3.

After a positive trigger decision is obtained, the data from the Beetle ASIC are read out on analogue links [21]. Each 128 channel Beetle ASIC provides four-output ports. The signals of 32 channels of the sensor and four channels of header information are sent serially at 40 MHz rate. The system has a maximum readout rate of 1.1 MHz. The data are sent out from the hybrid circuit board of the module on kapton cables, via vacuum feedthroughs to the repeater boards that are located outside the VELO tank. The analogue data are then transmitted over a 60 m long differential link (twisted pair) to the TELL1 DAQ boards. The TELL1 boards are located in the counting rooms outside the radiation zone.

The TELL1 DAQ boards digitise the analogue signals and process the data in FPGAs. The adjustment of the sampling phase is described in Sect. 3.2.1. The processing algorithms and the tuning of their parameters are described in Sect. 3.3. The TELL1 boards output the processed data to the high level trigger system [5]. The primary output from the TELL1 boards is zero-suppressed (ZS) data. For monitoring and tuning purposes, a number of special output data types can also be transmitted. The raw ADC values (non-zero suppressed, NZS) are sent out at a low rate of approximately 1 Hz. The data formats also contain the header data from the Beetle ASICs. The headers are used for the gain and error bank studies (described in Sects. 3.2.2 and 3.4 respectively).

### 3.2 Timing and gain

The ADC sampling time for the digitisation of the analogue data needs to be determined, as does the input gain of the digitisation boards. The ADC sampling time is set for each link to account, for example, for the slight differences in cable lengths. The gain in the ADCs is particularly important for the uniformity of the noise and signal levels measured subsequently. Then, the timing of the pulse sampling in the Beetle ASIC with respect

to the LHC beam collisions needs to be setup. These three calibration procedures are described below.

### 3.2.1 ADC sampling time

As described in Sect. 3.1, one triggered event of a VELO sensor is fully read out through 64 analogue links, that each carry 36 analogue voltage levels spaced by 25 ns each. The first four levels in this readout block are encoded header bits, which have their heights calibrated to be slightly ( $\sim 30\%$ ) larger than one MIP. On the receiving end, the TELL1 boards are equipped with cards that digitise the 36 consecutive levels, sampling every 25 ns. The sampling can be delayed by several clock cycles (25 ns) and fine time adjustments made with steps  $1/16^{th}$  of a clock cycle. The optimisation procedure first consists of roughly aligning the readout of the front-end signals to the digitising window. This is performed by sending internally generated signals, test-pulses, on known channels in the Beetle ASICs and adjusting the sampling so that the header bits are obtained in the correct positions. A scan is then performed over the fine time steps in order to get the final setting for each analogue link. The analysis of the scan data finds the optimal sampling point based on two conditions: the best signal to noise ratio and the minimal inter-symbol cross-talk. The inter-symbol cross-talk is defined as the fraction of the signal spilling over to the channel transmitted in the previous or next clock cycle on the same analogue link. A plot of the delay scan analysis is shown in Fig. 7, where the measured signal at each timing step is shown. The selected sampling point of the channels is indicated by the solid vertical line, while the small inter-symbol cross-talk at the sampling point of the previous and next channels is indicated with the dashed lines.

### 3.2.2 Gain

Each strip has a different capacitance, depending on its size and state of depletion, and the length of its routing line. This, in addition to the range of variances in the Beetle pipeline, cause links to have a range of signal sizes for a given deposited charge. The *gain* is normalised with a method that is independent of these variations and is stable as the VELO undergoes radiation damage. Here, gain refers to the conversion factor that relates a certain Beetle output voltage to an ADC value. The gain factor can be varied using a hardware setting on each digitisation card. This setting controls the upper limit of the voltage range digitised by the ADC and hence the proportionality of an input voltage to ADC counts.

The four bits of header information, which precede the 32 strip signals output on each link, encode the pipeline column number of the event. The headers are added to the link output in the Beetle, so they are not affected by strip capacitance or by non-uniformities in the Beetle pipeline. They are digital bits, which are subsequently sent over an analogue link, so can act as standard candles during the gain normalisation.

Depending on whether these digital bits corresponds to a ‘0’ or ‘1’, a header is classified as ‘Header High’ or ‘Header Low’, which when uncalibrated, typically have output values of around 560 and 460 ADC counts respectively. The distributions of high and low headers

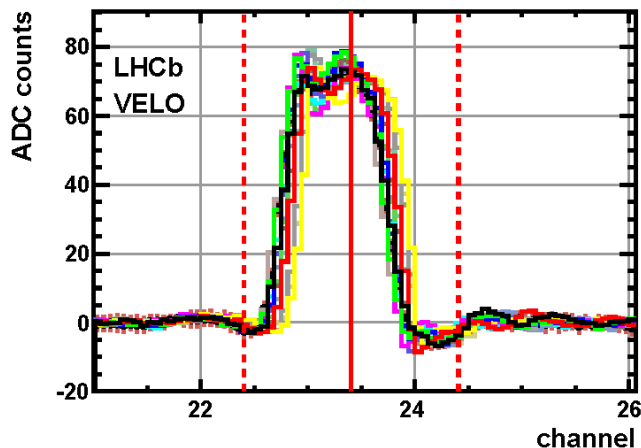


Figure 7: An example of the scan over the digitisation phases (see text). Data for 16 analogue links are shown. The horizontal axis represents the sampling time, where the integer numbers indicate the location of the serially transmitted Beetle channels, and between two channels there are 16 bins. The solid red vertical line indicates the chosen sampling point and the dashed red lines the position of the previous and next samples.

for each link are Gaussian in shape, and we define the full header swing (FHS) as the difference between the two means. To calibrate the VELO, the gain of each link is set to a value where FHS is equal to 100 ADC counts. The effect of a gain calibration on the FHS is shown in Fig. 8.

With the gain normalised, the most probable value of the Landau distributions and average noise values of each link are more uniform than for the uncalibrated VELO. The gain has been found to be fairly stable and the calibration procedure is repeated every six months or after the replacement of TELL1 digitisation cards or changes to the FPGA firmware.

### 3.2.3 Timing to the beam

After performing the digitisation and gain determination, a tuning is required to synchronise the front-end amplifier sampling to the signals generated in the silicon by particles from beam collisions. The signal left by a particle passing through a strip is pre-amplified and shaped in the Beetle ASIC. The level of this pulse is sampled every 25 ns and stored in a pipeline position. When a trigger command is received the Beetle outputs the data from the amplified signals that were sampled 4  $\mu$ s earlier; this trigger latency corresponds to 160 clock cycles. The time alignment adjusts the Beetle sampling time to the time that the particles pass through the detector, which is synchronous to the LHC bunch crossing time plus the time of flight of the particle to that sensor.

The time alignment is performed by scanning the clocks of the front-end readout in steps of 1 ns. Data from a few thousand collision events are stored for each step and the

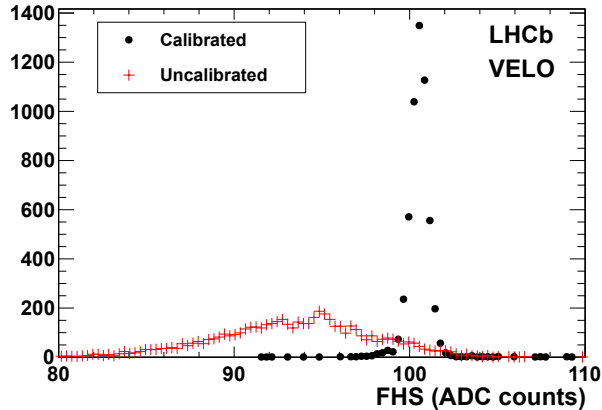


Figure 8: The FHS distribution before and after the first gain calibration. The data were taken two months apart in late 2009. One entry is made in the histogram for each link.

pulse-shape is reconstructed offline. The pulse-shape is fitted with a bifurcated Gaussian function, where the two halves have different widths but are constrained to have the same amplitude at the peak; this accounts for the difference in the rise and fall time of the pulses. This simple function does not fully describe the peak or the tails of the distribution, most notably the undershoot after the pulse, but gives good agreement in the rising and falling edges, and hence allows a quick and reliable way to optimise the sampling time. Conventionally the sampling time would be set to sample on the peak of the distribution, which would maximise the signal to noise distribution. However, we choose instead to minimise the contamination into the previous (pre-spill) or next (spillover) bunch crossing. This is obtained by setting a sampling time that equalises the spillover and pre-spill. As the rise time of the pulse is faster than the fall time this corresponds to sampling a few nanoseconds after the peak, and corresponds to a loss of about 4% in the optimal signal size. Figure 9 shows the result of a scan, with the simple function that is fitted shown and the optimal sampling time marked.

### 3.3 FPGA data processing algorithms

After digitisation the data are processed in a series of FPGA algorithms performed on the TELL1 board. Each TELL1 processes the output from one sensor, and contains four FPGAs each of which independently processes 512 channels of data.

A full bit-perfect emulation of the FPGA processing algorithms was implemented in C-code at the same time as the VHDL code for the FPGAs was developed. Extensive checks of the bit-perfectness are performed before any firmware changes, running both the TELL1 and C-code software on the same data samples and ensuring that bit-perfect agreement is obtained. The C-code emulation is then encapsulated, in a software project known as Vetra [22] used by both the VELO and LHCb Silicon Tracker, and run inside the

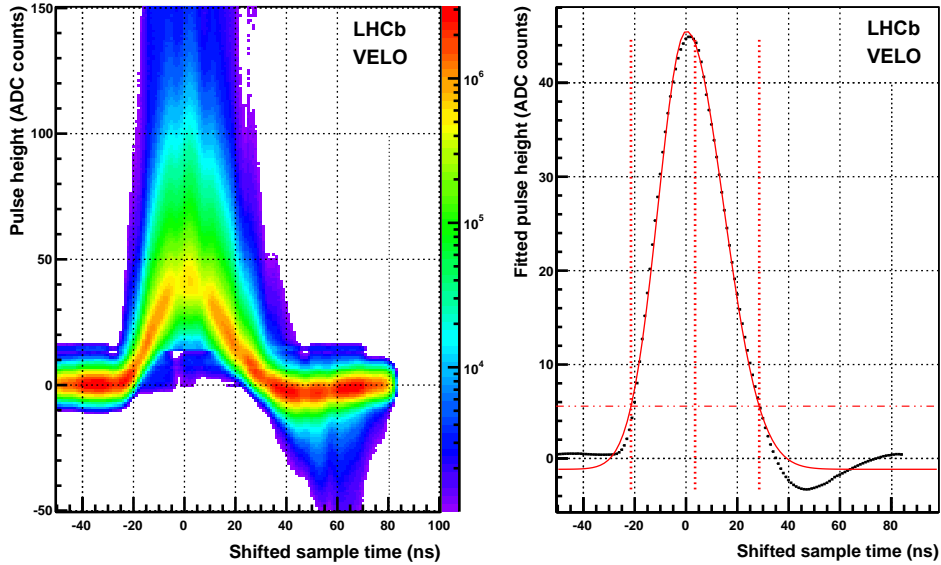


Figure 9: Pulse-shape obtained by combining data from all sensors, with a 1 ns time step and after applying for each sensor the time shift determined by the procedure. The plot on the left shows the ADC spectra versus time. The plot on the right shows the most probable value for each time bin obtained from a fit of a Landau convolved with a Gaussian function. A bifurcated Gaussian function is fitted to this distribution from which the rise and the fall widths are obtained. The fitted function also predicts the amount of pre-spill (25 ns before the chosen point) and the spillover (25 ns after), which are marked with red vertical dotted lines. The chosen sampling time is also marked with a red vertical dotted line.

main software framework of the experiment. This allows the algorithms to be fully tested with data before being deployed in operation for collision data. This also allowed the algorithms to be fully tested and debugged during the commissioning period. In operation, the ability to fully emulate the processing steps allows the output of any processing stage to be monitored, which is used for assessing the data quality and fully understanding the system performance.

The algorithms described below require a set of tuneable parameters to be determined and uploaded to the FPGAs. The parameter values used are stored in XML files and recorded in a database. The parameters are primarily based on the analysis of NZS data using the Vetra package. For example, the pedestal values are determined and the cluster thresholds are optimised. In total 550k parameters are stored in the XML files for operation of the system.

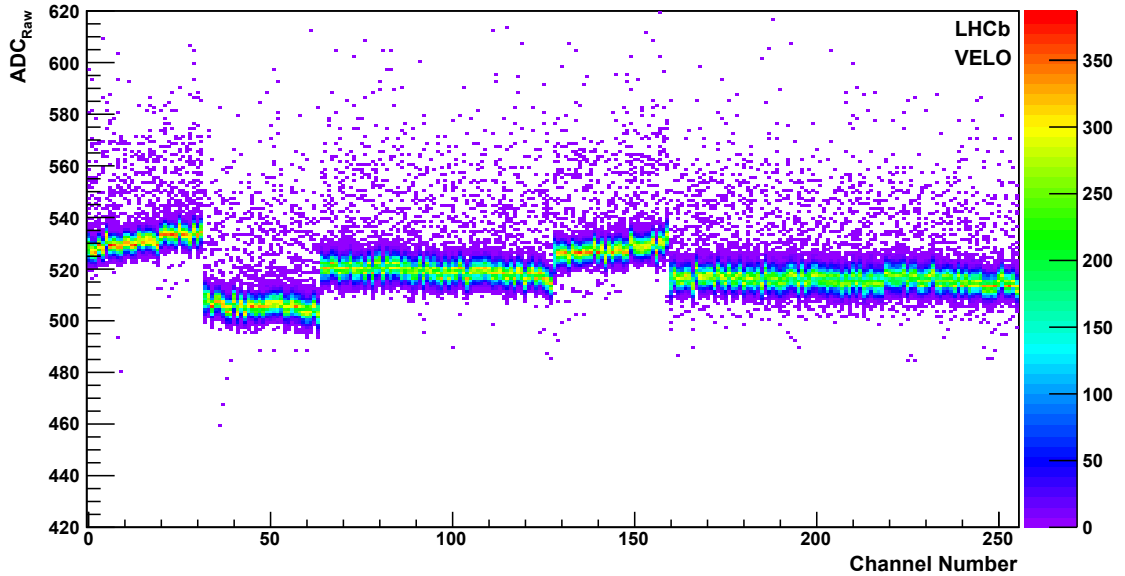


Figure 10: Typical raw (Non-Zero Suppressed) data ADC values. Data from two ASICs, each with four analogue links, is shown. Variations in the pedestal values at the ASIC, analogue link, and channel level are seen.

### 3.3.1 Pedestal subtraction

Significant variation in the average raw ADC values (pedestals) are observed for each Beetle ASIC. Variations in pedestal from link-to-link and channel-to-channel for the raw NZS data are also seen, as shown in Fig. 10. Hence, the pedestal values must be determined for each channel of the system individually, and thus 180k 10-bit pedestal values are required.

The pedestal values are determined offline using NZS data collected when there are no collisions. The values are then uploaded to the FPGAs, and are subtracted from the raw ADC when processing each event. Operational experience has shown that the pedestal values remain relatively stable and a pedestal retuning is made once the pedestal subtracted ADC values of more than a few percent of channels are more than 2 ADC counts away from 0. A retuning typically happens every two months, and is usually performed during technical stops of the LHC. A retuning is also required after the replacement of a TELL1 digitisation card or a change to the firmware. In addition to the pedestal subtraction, channels in the system that are known to be faulty are masked at this stage of the data processing.

### 3.3.2 Mean common mode suppression

The 128 channels of the sensor that share the same Beetle ASIC, and the 32 channels of one analogue link may be subject to the same sources of signal fluctuation, known

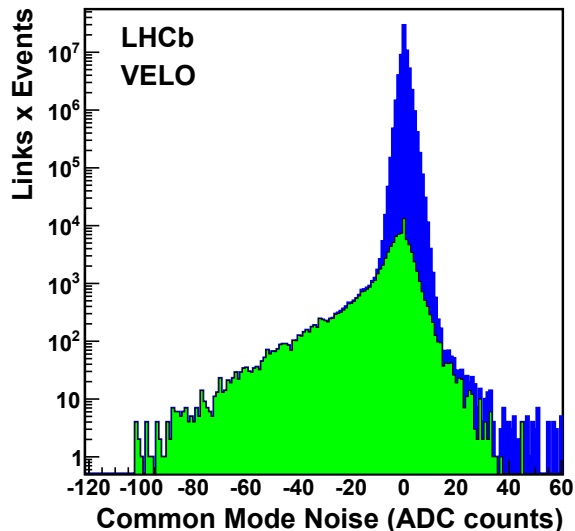


Figure 11: Distribution of common mode noise per link. The blue histogram is for all links. The green histogram is for links in a ASIC that has large signals (see text).

as common mode (CM) noise. The CM noise is suppressed in the FPGAs with a Mean Common Mode Suppression (MCMS) algorithm which operates on each analogue link, correcting any baseline offset in each event.

In the algorithm, first the average pedestal-subtracted ADC value of the channels in a link is calculated for that event. Using this mean value a search for particle hits is performed for each channel. All channels with hits are masked, and a new mean value is calculated for each link. This value is then used to correct the ADC values in all channels of the link.

This algorithm would not fully correct common mode sources from the silicon sensor, for example from noise pickup from the proton beams. This is because consecutive channels on the sensor are not read out on consecutive inputs of the front-end ASIC (see Sect. 3.3.3). A second common mode algorithm was originally foreseen for use after channel reordering. However, studies performed by monitoring the noise level as a function of the VELO opening distance, showed that this source of noise pickup was small, and this second common mode algorithm has not been used in operation.

Figure 11 shows the distribution of the CM noise measured in the system. It peaks at 0 and has a sigma of 1.74 ADC counts. Furthermore, out of the 1.74 ADC counts link CM noise, there is a common fluctuation among all 5376 links, introduced by the common power supply and environment. This global common mode noise is 1.47 ADC counts, meaning the intrinsic link common mode noise is 0.93 ADC counts. For comparison the average incoherent (CM suppressed) noise is 1.91 ADC counts.

The common mode distribution has a long tail on the negative side, where all four



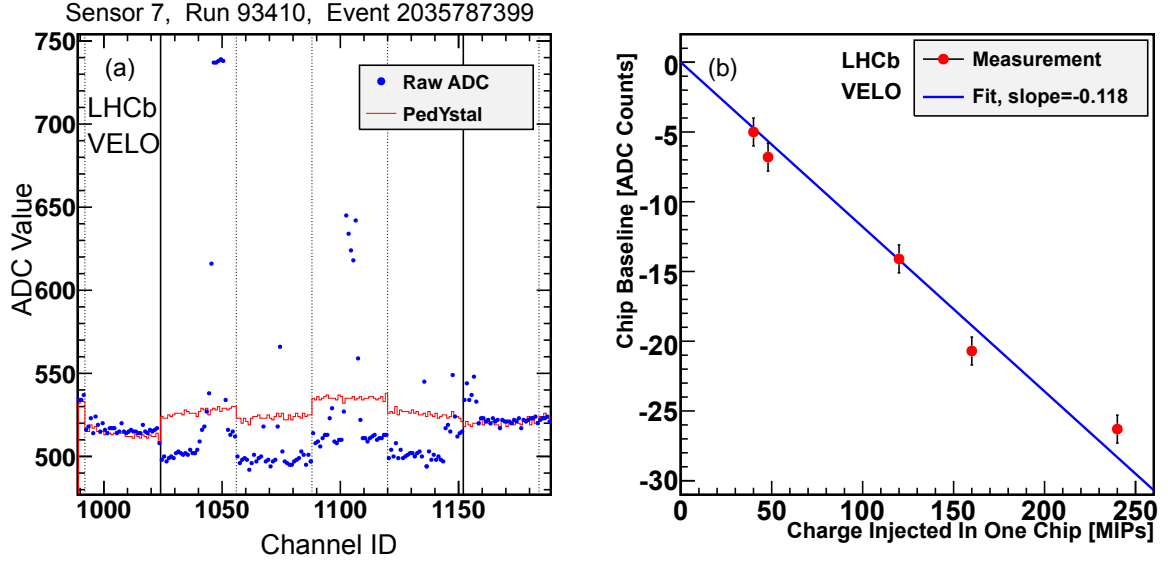


Figure 12: (left) Event snapshot for an ASIC that has large signals (channels 1024-1152). The blue dots are the raw ADC values. The red lines are the pedestals. (right) ASIC baseline shift in response to injected charge in units of the most probable charge deposited by a MIP in 300  $\mu\text{m}$  thick silicon.

links from the same ASIC have a coherent baseline shift. The effect is illustrated in an event snapshot in Fig. 12 (left). Accompanying the baseline shift are a few channels with very large signals that reach the saturation point of the electronics, most likely arising from soft tracks at large angles. In Fig. 11 the green distribution corresponds to links that have at least two channels with signal more than 180 ADC counts above the baseline. The large energy deposition hypothesis was confirmed in a test-pulse calibration procedure. A controllable amount of charge is injected to a few selected Beetle ASIC channels using test-pulse calibration capacitors. The baseline shift is proportional to the injected charge as shown in Fig. 12 (right). These baseline shifts are corrected by the CM correction algorithm.

### 3.3.3 Topological strip channel reordering

As a consequence of the layout of the routing of the channels from the VELO  $R$  and  $\Phi$  sensors on the second metal layer, neighbouring channels on the sensor are not necessarily read out consecutively. In the  $\Phi$  sensor strips from the inner region of the sensor are routed out over strips in the outer region, and the readout is thus intermingled between inner and outer region strips, as shown in Fig. 2. Therefore the electronic readout ASIC channel numbering does not correspond to the physical (strips) channels on the sensors. The zero-suppression and clusterisation must be performed in terms of physically neighbouring channels, and thus a translation algorithm is necessary. The reordering procedure is

performed separately for  $R$  and  $\Phi$  type sensors. The implementation of this algorithm consumes a significant amount of the FPGA resources.

### 3.3.4 Zero suppression and clusterisation

The final data processing algorithm on the TELL1 produces the raw cluster bank which is sent out to the high level trigger. This processing reduces the data size by only transmitting channels that have significant signals present. It also groups together neighbouring hits that may be due to single particles and produces a first estimate of the centre of this cluster.

In the first step, hit detection is performed by finding signals above seeding thresholds. The current seeding threshold in each channel is set to be six times higher than the measured noise in that channel, rounded to the nearest ADC count. This limits fake noise hits while not significantly reducing the selection efficiency of true signal clusters in fully depleted sensors (see Sect. 4.1).

In the second step, the algorithm attempts to include adjacent strips in the cluster. Strips are added to the cluster if they pass an inclusion threshold, which is currently set at 40% of the seeding threshold. By setting a lower inclusion threshold than the seeding threshold additional charge is added to the cluster, which helps improve the resolution on the particle position. The maximum number of strips per cluster is four.

The centre of the cluster is calculated from a pulse-height weighted average of the strips contributing to the cluster. This is calculated with a precision of an eighth of a strip (3-bits). This calculation is used to save time in the trigger; it is recalculated with floating point precision for use in the offline tracking. The resolution and cluster detection efficiency are discussed in Sect. 4.

Finally, each cluster is encoded into a bit structure that contains information on the cluster position, cluster size, and the charge measured on each strip that contributes to this cluster. The size of the raw cluster bank varies depending on the event's occupancy, and the typical size of this bank for the full VELO is about 20 kB.

## 3.4 Error identification

Information is sent out from the Beetle in the header bits that allow a number of consistency checks to be performed. Error banks are then produced by the TELL1s when the data of a link is internally inconsistent, or there is inconsistency between data from various links. They aim to contain the required information to trace down the origin of the error and take appropriate measures. The most commonly occurring errors relate to the verification of the pipeline column number. This number records in which column of the Beetle pipeline the data are stored while awaiting a first level trigger acceptance signal. The pipeline column number is reset periodically by a broadcast command and hence verifying that it is identical for all front-end ASICs ensures the synchronicity of the detector. Elements of the binary value of the pipeline column number are transmitted as an analogue signal preceding the data from each link of the ASICs. Gain variations and inter-symbol cross-

talk can cause the analogue values to end up in between the corresponding low and high bit thresholds, and consequently make the bit assignment ambiguous. Calibration and verification procedures that are executed regularly, have managed to control these effects to a satisfactory level and errors now occur at the level of a few in every ten thousand events.

### 3.4.1 Single event upsets

One error type of particular interest is a single event upset (SEU). Since the Beetle ASIC is exposed to ionising radiation charge will be liberated in its electronic circuits. Most particles will however not generate enough charge to influence the operation of the devices. Occasionally a highly ionising particle can cause a change in the logic state of one of the flip-flops in the Beetle ASIC. These SEU can affect the performance on the ASIC if they occur for instance in one of the configuration registers. Therefore all critical flip-flops are implemented in a triple redundant way, featuring majority voting and auto-correction. To monitor the rate of SEU, all bit-flips are counted in a dedicated counter. The two least significant bits of this counter are sent with the data for every trigger as part of the header bits. By analysing the transitions of these counter bits, an average of 2.9 SEU per  $\text{pb}^{-1}$  of delivered integrated luminosity for all 1344 Beetle ASICs combined is observed.

## 3.5 Monitoring

The VELO monitoring infrastructure is used to ensure that any degradation in data quality is observed and can be followed up quickly. It is complementary to the LHCb monitoring which is split in two components: online and offline monitoring. The LHCb online monitoring analyses a fraction of the ZS data sample that has been selected by the trigger. The LHCb offline monitoring uses a number of lightweight algorithms to monitor a sample of all data that are processed for physics analyses. The VELO monitoring adds two components: an analysis of NZS data and a detailed analysis of the ZS data. Experience shows that many data quality problems are spotted first in the detailed checks performed by the dedicated VELO monitoring team.

The NZS data are recorded in a special data stream which is stored separately from the physics data at a rate of 1 Hz. Events directed to this stream contain NZS data from all VELO sensors. This allows the analysis of pedestals, common mode suppression, cross-talk effects and noise to be made for each run. The NZS readout has also been used to study correlations between different sensors in the same event (see Sect. 3.3.2).

The VELO monitoring also analyses ZS data which have not been biased by any trigger selection. This sample of events is thus representative of the data being recorded by the detector, and allows the detector performance to be monitored independent of changes to the trigger. These data are recorded at a rate of 10 Hz and stored in a separate data stream to increase the efficiency of the data analysis.

All data in the ZS and NZS streams used by the VELO monitoring are processed automatically by monitoring algorithms shortly after they have been recorded. The output

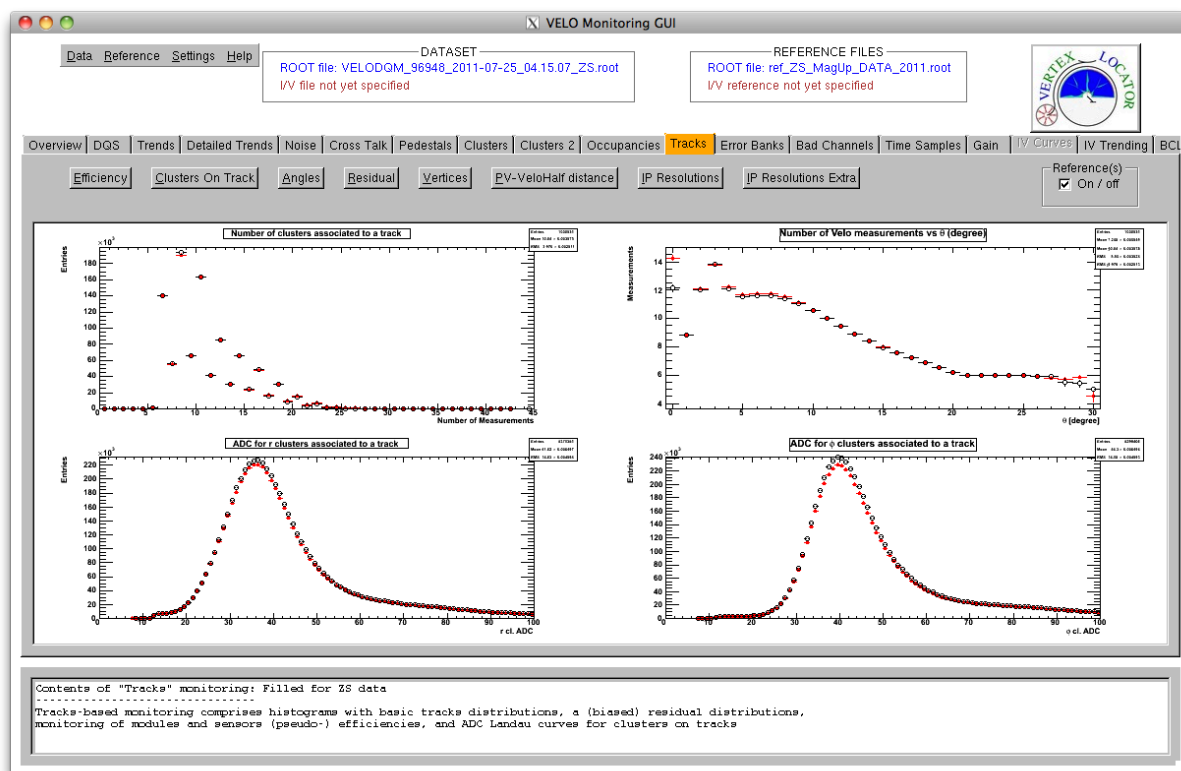


Figure 13: Example of the graphical user interface used in the VELO monitoring. Shown are distributions of the number of hits per VELO track segment (top left), the track angle with respect to the beam axis (top right), and the ADC counts of  $R$  and  $\Phi$  sensor clusters associated to a track (bottom left and right, respectively). The results of the current run are shown in red filled symbols and the reference data for comparison are shown as black open symbols.

of the monitoring algorithms are analysed daily by VELO data quality shifters. These are people on call who analyse the incoming data and alert experts of problems if necessary. These analyses include information on pedestals, noise, common mode, cluster signal distributions, occupancy, tracking and alignment. Separate monitoring is implemented for all slow control data such as voltages, currents, temperatures and pressures.

A graphical user interface has been developed to facilitate the analysis of the output of the regular monitoring algorithms. An example of its usage is shown in Fig. 13. The same tool also produces trend and correlation plots of the relevant quantities, which are used to track the detector stability over time. Summary tables of representative values to assess data quality, for example numbers of high occupancy channels, for each run are also made. The summary values and comments from the analyst of the data are stored in a dedicated electronic logbook.

Data are also taken under special conditions to cover aspects that cannot be easily accessed with physics data. Dedicated monitoring is in place for these periodic performance checks. These include sensor current versus voltage, current versus temperature, noise

versus voltage, and charge collection efficiency versus voltage data which are performed to monitor radiation damage (see Sect. 4.6).

### 3.6 Simulation

The LHCb simulation is based on Monte-Carlo event generators and the use of the GEANT4 toolkit [18]. A detailed model of the detector material in the VELO has been produced, through which the simulated particles are propagated (see Sect. 2.6). The entry and exit points of the simulated particles in the silicon sensors are obtained from GEANT4. A thin silicon sensor is expected to have an energy deposition distribution that can be described by a Landau function convolved with a Gaussian distribution. The charge deposited by a particle in the silicon sensor is calculated using the form from theory and previous experiment [23].

The total deposited charge is distributed at uniformly spaced nodes along the particle path in the silicon, with the energy fluctuations along the path simulated. The diffusion of the charge as it drifts in the electric field of the silicon is simulated through a Gaussian smearing whose width is dependent on a bias voltage parameter. Cross-talk between the charge attributed to the strips is then added to model capacitive coupling. Noise is added to the strips following the measured values in the data. The measured pulse-shape of the front-end electronics is also simulated, and corrections are applied for the time of flight of the particles. The electronics response from the previous and the next events are also simulated by applying the pulse-shape to simulated events. Pedestal offsets and common mode noise are not normally simulated as they are removed effectively in the real data by the FPGA processing algorithms. This simulation stage results in a model of the amount of charge collected on a sensor's strips. The model has the bias voltage and capacitive coupling as free parameters which are tuned to obtain agreement with the measured data resolution as a function of pitch and track angle and typically agree to within 5%. This simple algorithm is fast and sufficiently accurate for the simulation required for physics analyses.

The next stage of the simulation models the processing in the TELL1 board. First, the signal is digitised. At this point the DAQ emulation produces an output format that corresponds to the raw non-zero suppressed data. The simulated data are then passed through the bit-perfect emulation of the TELL1 clusterisation algorithm (see Sect. 3.3). Identical clusterisation thresholds are used to those in the data taking. The output data bank is then produced in the same format as that produced by the TELL1 boards. A global scaling, the gain (electron to ADC conversion), is applied to normalise the observed signal in simulation, with a correction for the variation in signal size with radius (see Sect. 4.1). The trigger, pattern recognition and track reconstruction algorithms are applied identically for real and simulated data.

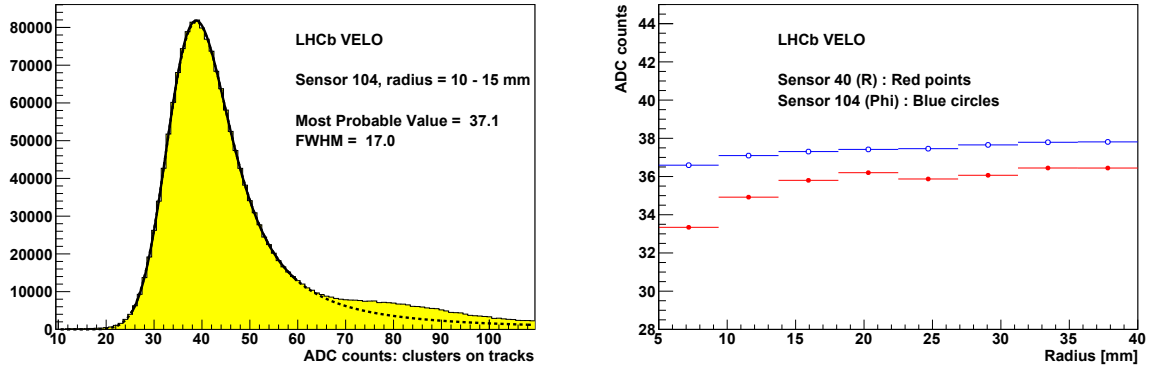


Figure 14: (left) Fit of the signal distribution for Sensor 104 (a  $\Phi$  sensor) for clusters on long tracks with a track intercept point on the sensor  $10 < r(\text{mm}) < 15$ . (right) The most probable value of the fits to sensors 40 and 104, the  $R$  and  $\Phi$  sensor of the same module respectively, as a function of the track intercept point radius. The cluster ADC counts were normalised to a track crossing  $300 \mu\text{m}$  of silicon.

## 4 Overall system performance

This section characterises the VELO system performance, including the signal to noise ratio, hit resolution, occupancy, and efficiency studies. Beam backgrounds are also discussed. The results presented use data before appreciable effects of radiation damage were observed, results on the observed radiation damage are reported at the end of this section.

### 4.1 Signal size and noise rate

The observed total signal from the clusters is determined by fitting a Landau convolved with a Gaussian function around the peak region. The deposited charge for each track is corrected for the track's angle to give a result corresponding to a path length in the silicon of the nominal  $300 \mu\text{m}$  thickness of the sensor. An example fit is shown in Fig. 14 (left). The function provides a good description of the rising edge and peak region, but undershoots the data in the high energy deposition region. This is in part due to the presence of photon conversions to electron positron pairs which, in the absence of an appreciable magnetic field in the VELO, can remain merged into a single cluster. The tuned simulation is in good agreement with the data distribution, including in the high energy deposition region, and the FWHM does not require any additional smearing of the detector response. The most probable value (MPV) of the Landau distribution varies as a function of track radius, as shown in Fig. 14 (right).

The noise of the front-end ASIC depends on the strip capacitance. On the  $R$  sensors the inner radius strips have the lowest capacitance due to their shorter length though this is partially compensated due to the inner strips having longer routing lines. Still, the

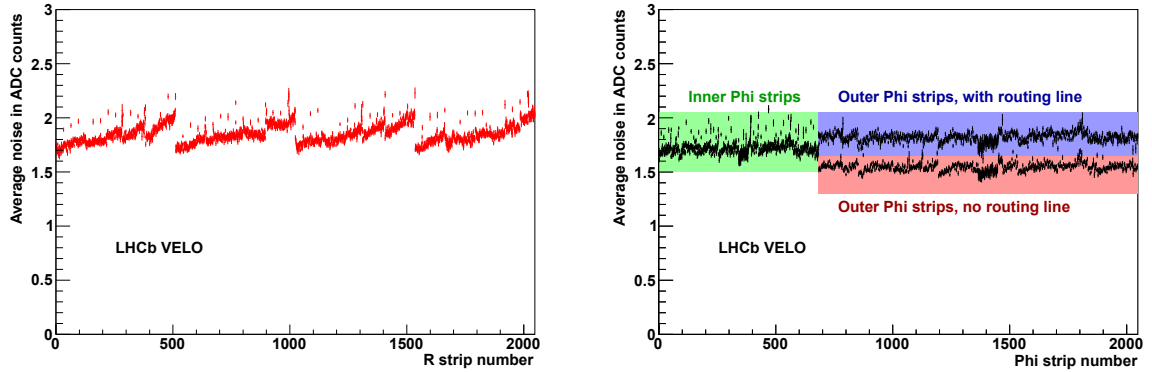


Figure 15: Noise in ADC counts averaged across the 42 installed  $R$  (left) and  $\Phi$  (right) sensors, with the error bars indicating the RMS of the distribution.

dependence of the noise on the strip length is visible when comparing Fig. 15 (left) with the sensor layout shown in Fig. 2. The  $R$  sensor is divided into four approximately  $45^\circ$  segments, and the strip length increases with increasing strip number in each segment. The  $\Phi$  sensor has two zones with inner and outer strips. The inner strips are shorter but have additional routing line contributions to their capacitance. In the outer zone every alternate strip is under the routing line for an inner strip so the capacitance for these strips is larger. The noise in these three types of  $\Phi$  sensor strips is shown in Fig. 15 (right). Larger noise is also clearly visible in both the  $R$  and  $\Phi$  sensors every 32 channels, this is due to inter-symbol cross-talk from the digital header information into the first channel in each analogue readout link. A suppression algorithm for this inter-symbol cross-talk has been implemented in the FPGAs, but is not currently used due to the small size of this cross-talk and the large signal to noise ratio.

The average signal to noise ratio, computed as the average MPV of single strip clusters divided by their strip noise, for the VELO is around 20:1. It is higher for the  $\Phi$  sensors than the  $R$  sensors and shows a variation on the sensor radius as shown in Fig. 16.

## 4.2 Resolution

The hit resolution in silicon devices depends on the inter-strip readout pitch and the charge sharing between strips. The charge sharing varies with operational bias voltage and the projected angle of the track. The bias voltage was 150 V throughout the physics data taking in 2010–2012. The projected angle provides information on the number of strips that the particle crosses while it traverses the thickness of the silicon sensor. It is defined as the angle between the track and the perpendicular to the sensor, in the plane perpendicular to the sensor and containing the perpendicular to the strip. Initially the resolution improves with increasing angle, due to the charge sharing between strips allowing more accurate interpolation of the hit position. The optimal resolution is obtained

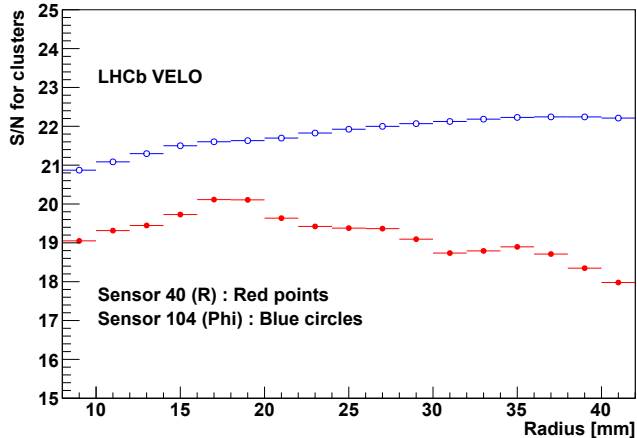


Figure 16: Signal to noise (S/N) ratio from the MPV of the signal for single strip clusters on tracks divided by the noise of that strip. Shown are the S/N values for sensor 40 (R) and sensor 104, the  $\Phi$  sensor of the same module, as a function of impact point radius.

when the tracks cross the width of one strip when traversing the  $300\ \mu\text{m}$  thickness of the sensor. For the VELO the optimal projected angle varies between about  $7^\circ$  at the lowest inter-strip pitch of  $40\ \mu\text{m}$ , to about  $18^\circ$  for the largest  $100\ \mu\text{m}$  pitch strips. Above the optimal angle the resolution begins to deteriorate due to the fluctuations in the charge on the strips and because the signal to noise ratio on individual strips may drop below the clustering threshold.

The clustering algorithm and charge interpolation method is described in Sect. 3.3. The VELO reads out analogue pulse-height information from the strips, and this information is used offline to calculate the cluster position using the weighted average of the strip ADC values. Including the track angle dependence in the clustering algorithm is found to give a small improvement in precision. The results presented here rely on the offline recalculation of the position, while the trigger relies on the lower resolution (3-bits) calculation (see Sect. 3.3.4). The estimated resolution in the simulation is parameterised and fitted as a function of both track angle and strip pitch. This resolution estimate for each hit is then used in the Kalman fit tracking algorithm.

The hit resolution is determined from the hit residuals which are evaluated using the LHCb Kalman filter track fit [24] and include a correction for multiple scattering and energy loss dependent on the track momentum. The residual is defined by the distance between the hit measurement and the extrapolated point of the fitted track to that sensor. As the hit for which the residual is being determined is included in the track fit this gives rise to a bias in the residual which must be corrected for. The bias correction used to determine the residual is  $\sqrt{V_M/V_R}$  [25] where  $V_M$  is the variance of the measurement and  $V_R$  is the variance of the residual. The evaluation of this correction is implemented in the Kalman fit.



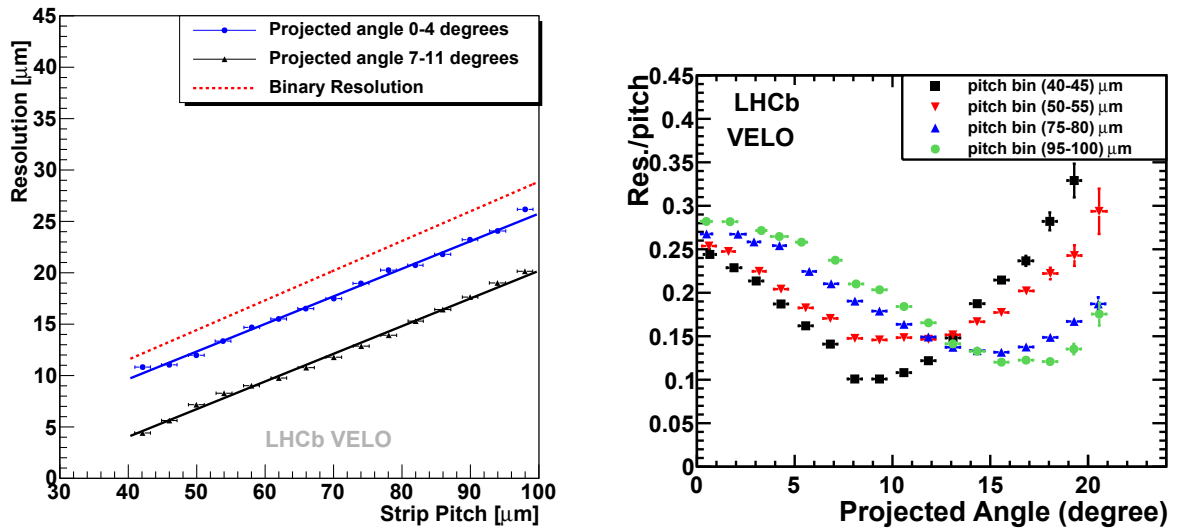


Figure 17: (left) The VELO resolution for two projected angle bins for the  $R$  sensors as a function of the readout pitch compared with binary resolution. (right) Resolution divided by pitch as function of the track projected angle for four different strip pitches.

The resolution has been determined as a function of the strip pitch and of the projected angle. For each bin, the resolution has been determined from the sigma of the fit of a Gaussian function to the distribution of the corrected residuals. The resolution is evaluated using tracks that have hits in the tracking stations behind the magnet and hence for which the momentum measurement is available. The tracks are required to have a momentum greater than  $10 \text{ GeV}/c$  to reduce the dependence on the estimation of the multiple scattering effect, and a number of other track quality criteria are applied to reject fake tracks. The results are presented here for the  $R$  sensor. The  $\Phi$  sensor results are compatible but the almost radial geometry of the strips means that tracks primarily have small projected angles.

The measured hit resolution has a linear dependence on the strip pitch in projected angle bins, as shown in Fig. 17 (left). The hit resolution at small projected angles, almost perpendicular to the sensor, has a resolution which is close to that which would be obtained from a binary system. This is to be expected as the charge sharing between strips at this angle is minimal. A significantly better resolution is obtained for larger projected angles, where the fraction of two strip clusters increases and the analogue readout of the pulse height in each strip is of benefit. The hit resolution as function of the projected angle is shown in Fig. 17 (right) and the fraction of one and two strip clusters as a function of the projected angle and strip pitch are shown in Fig. 18. The best hit precision measured is around  $4 \mu\text{m}$  for an optimal projected angle of  $8^\circ$  and the minimum pitch of  $40 \mu\text{m}$ .

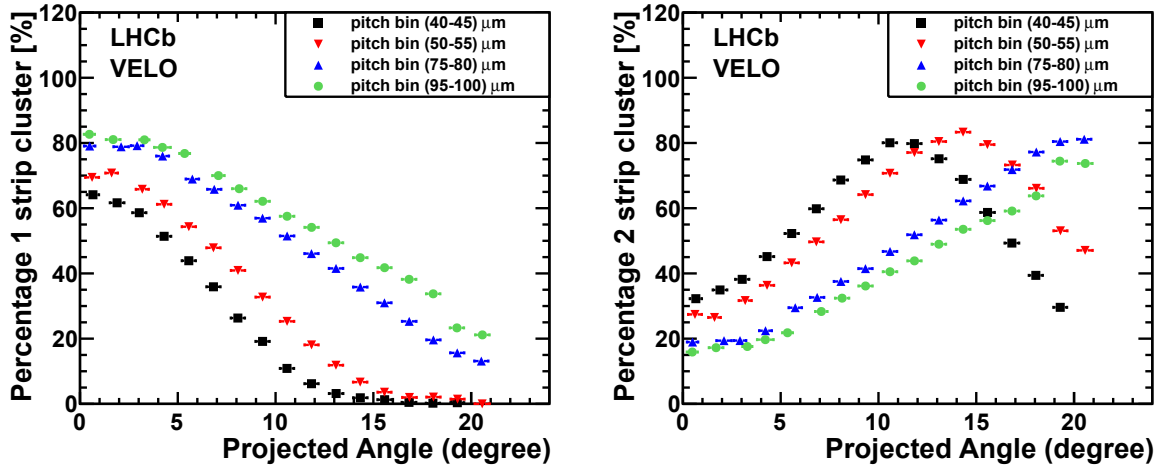


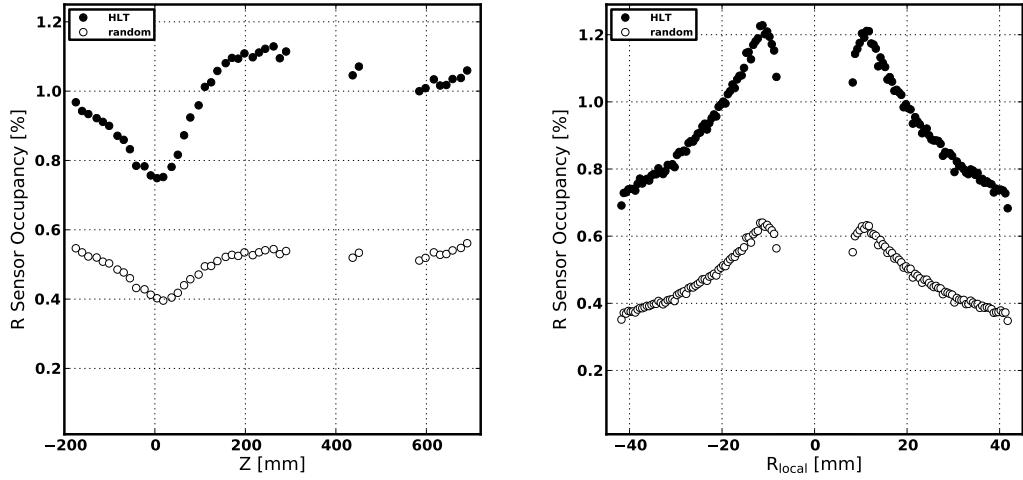
Figure 18: The percentage of one (left) and two (right) strip clusters as a function of the track projected angle for four different strip pitches.

### 4.3 Occupancy

The detector occupancy is a key parameter in the performance of the pattern recognition and tracking algorithms of the experiment. High occupancy can lead to the mis-identification of hits on tracks and increase the number of hit combinations decreasing the speed of the algorithms. The occupancy shown here is for clusters. The cluster seeding thresholds and masking of noisy strips in the FPGA data processing algorithms ensure that the contribution to the occupancy from noise is negligible compared with that from particles; in the absence of circulating beams the observed occupancy is below 0.01%. The typical cluster occupancy during 2011 operations is shown in Fig. 19 (top plots). Only events from particle beam crossings are utilised in the computation, and this data sample has an average number of visible interactions per beam crossing,  $\mu$ , of 1.7. The occupancy is shown computed with data collected using two different triggers. Data from a random trigger on beam crossings are used as this represents the average occupancy in the events observed by the detector. The occupancy for events passing the high level trigger is also given, this is higher as events with heavy flavour production are typically of higher multiplicity than the average. The distribution for events passing the high level trigger is not fully symmetric around the collision point due to the preference of selecting events in the LHCb acceptance.

The cluster occupancy has a dependence on the position of the sensors along the beam-line, as shown in Fig. 19 (left). The location of the interaction region is clearly visible from the dip in the occupancy distribution. The highest occupancy of 1.1% for events passing the trigger is at around the end of the closely spaced region of sensors in the VELO, where the occupancy is 44% larger than at its minimum.

The occupancy also varies across the sensor, increasing closer to the beam as seen



### LHCb VELO

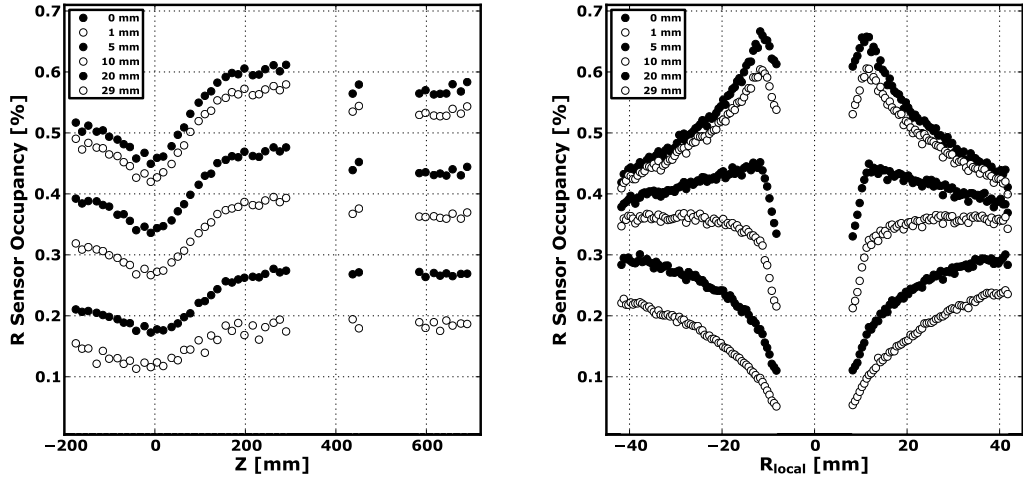


Figure 19: Cluster occupancy in the VELO silicon strip detectors. (left plots) Average occupancy in the sensor as a function of the position of the sensor along the beam-line. (right plots) Occupancy as a function of the local radius of strips on the  $R$  sensors, with a negative sign applied to sensors on one half. The upper plots show the occupancy when fully closed using 2011 data with a  $\mu$  of 1.7 and for events selected using a random trigger or with events passing the high level trigger. The lower plots show the occupancy as a function of closing distance with fully closed labelled as 0 mm, the points below then follow in order of the retraction distance indicated in the key.

in Fig. 19 (top right). The maximum occupancy is 83% higher than the minimum as a function of  $R$ . This is a much weaker dependence than might naively be expected since the inner strips are five times closer to the beam than the outer strips. However,

the semi-circular sensor geometry means that the strip length naturally reduces with decreasing radius on the  $R$  sensors, and the inter-strip pitch also reduces with decreasing radius on both the  $R$  and  $\Phi$  sensors. The occupancy reduces in the smallest radius region on the  $R$  sensors as these strips are shorter due to having the corners cut off.

Figure 19 (lower plots) also shows how the occupancy varies across the sensor at a range of closing distances. These data do not have a well defined  $\mu$  as the luminosity levelling (see Ref. [26]) had not yet been performed. The minimum average sensor occupancy drops from around 0.4% when closed to around 0.1% when the VELO sensors are fully retracted by 29 mm from the beam. Even in the fully retracted position the number of particles that can be reconstructed in the detector allows the performance of the system to be determined and the primary vertex to be fitted to allow the detector to be safely closed (see Sect. 2.5).

#### 4.4 Beam backgrounds and high multiplicity events

Studies have been performed of beam-related backgrounds in the VELO, and a number of sources of hits have been identified: beam-gas interactions; instrumental effects triggered by the presence of beam; and beam interactions with collimators. The rate of these effects is sufficiently low to not have a significant detrimental effect on physics or to contribute significantly to radiation damage in the detector.

The interaction of beams with residual gas in the LHC vacuum pipe and VELO vacuum vessel provides a useful data sample for alignment and luminosity studies. Simulations of beam-gas interactions in the VELO vacuum vessel and the long straight section of the LHC have been performed [27], with the latter including particle fluxes from beam-gas interactions in the long straight section and from proton interactions in collimators. Tracks arising from these beam-gas interactions provide a complementary sample to tracks from beam-collisions due to their very forward angular distribution. Many of these tracks pass through all VELO sensors and this provides useful additional constraints for alignment (see Sect. 5.2). The reconstruction of the beam-gas interaction vertices in the VELO region is illustrated in Fig. 20 (left). The blue and red points are obtained from events in which only one beam passed through LHCb, and vertices with at least five tracks are reconstructed from interactions of the beam with residual gas. The horizontal crossing angle of the beams is apparent. The downstream beam (red) interactions are limited in their extent in the negative direction along the beam-line by the predominantly forward acceptance of LHCb. This reconstruction of beam-gas interactions allows a measurement of the transverse bunch profile along the beam trajectory to be obtained and allows the beam angles, profiles and relative positions to be determined. The beam-overlap integral can then be obtained from the extracted beam profiles and has been used to obtain a measurement of the luminosity [28]. The precision of the VELO allows this luminosity determination to be performed with a comparable precision to that obtained from the well-known van der Meer scan method. The rate of beam-gas interactions can also be increased in the VELO by the use of a gas injection system, which was commissioned in 2011 [29].

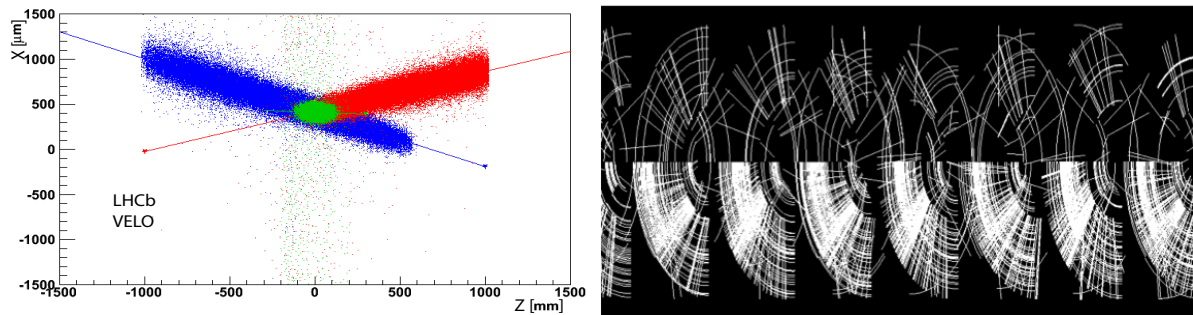


Figure 20: (left) Imaging of the LHC beams through the reconstruction of the production vertex of tracks in 2010. The vertices from beam-gas interactions with the beam travelling in the  $+z$  ( $-z$ ) direction in LHCb are shown in blue (red). Vertices arising from beam-beam interactions are in green. The vertical axis represents the horizontal direction ( $x$ ) and the horizontal axis the beam direction ( $z$ ). (right) An event display image showing clusters in  $R$  and  $\Phi$  sensors with a high occupancy in a localised region assumed to be due to a beam background splash event.

Events containing a collimated spray of background hits are also observed, as shown in Fig. 20 (right). These events are characterised by high occupancy in local regions of the sensor, and they are correlated with activity in other tracking detectors. The rate of events is proportional to the beam intensity in the LHC, and typically constituted 0.03% of events passing the high level trigger in 2011. A possible origin for these events is beam interactions with collimators.

## 4.5 Efficiency and faulty channel analysis

Studies have been performed of the charge collection efficiency and cluster finding efficiency of the detector. The detector is initially operated at a bias voltage sufficient to obtain the full charge from the sensors, and the charge collection efficiency and cluster finding efficiency as a function of radiation are reported in Sect. 4.6. In addition faulty channels have been identified through the study of the cluster finding efficiency, occupancy and noise spectrum.

The cluster finding efficiency is a useful measure of the performance of the detector. This is determined by excluding a sensor in the pattern recognition, and interpolating tracks to this sensor. The tracks are required to have hits in both the  $R$  and  $\Phi$  sensors in the two modules before the test sensor and in the two modules after the test sensor. These requirements place some restrictions on the sensors that can be probed and the regions analysed within the studied sensors. Tracks that have intercept points inside the active region of the sensor are then considered. Track quality selection cuts are applied to remove fake tracks and track isolation cuts to prevent a cluster from another track being selected. The efficiency with which clusters are found near the track intercept points is then determined. The efficiency for finding a cluster depends on the applied bias voltage and the thresholds applied in the cluster making algorithms. The standard operational

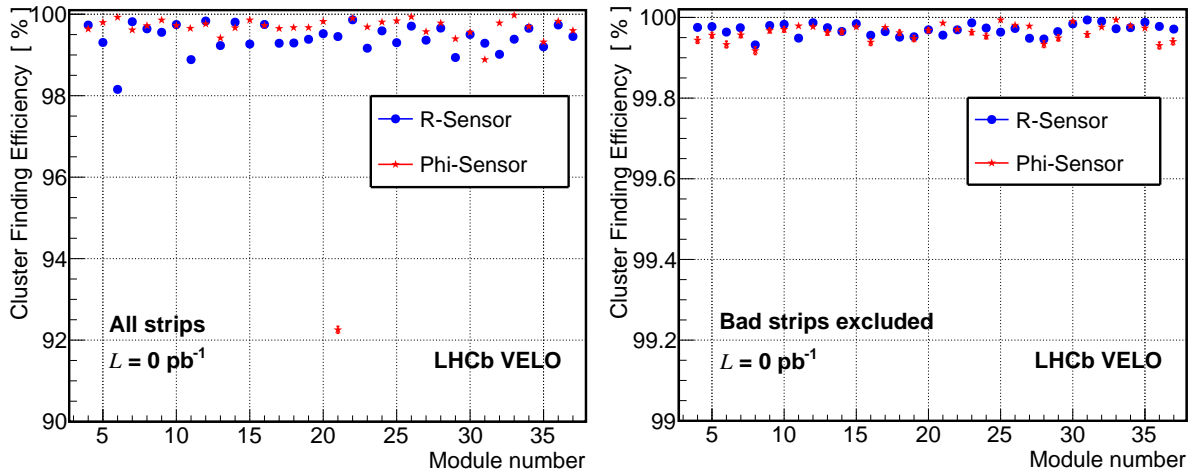


Figure 21: The cluster finding efficiency for each sensor with all strips (left) and when identified bad strips are excluded (right).

settings are used for the studies presented here.

The region boundary between the inner and outer strips of the  $\Phi$  sensor and the middle region boundary of the  $R$  sensor both contain a  $79 \mu\text{m}$  wide region with the HV bias resistors. This region and the region of the guard ring around the sensor are excluded in the efficiency calculation. Averaging across sensors, cluster finding efficiencies of 99.45% sensors were obtained at the start of operation as shown in Fig. 21. Bad strips are identified with the cluster finding efficiency analysis described below. When these bad strips are neglected the cluster finding efficiency rises to 99.97%. The system contains only a single front-end ASIC that is not functioning, the failure of which occurred after production and before the start of physics operations, this is visible in the reduced efficiency of the  $\Phi$  sensor of module 21 in Fig. 21 (left).

During the production of the modules faulty channels were identified through the application of three techniques: high resolution visual microscope inspections, the response of the modules to scans of a laser, and the analysis of noise data. A total of only 0.6% of the VELO sensor strips were found to be faulty, see Table 1. The analysis of noise data can also be performed on the installed experiment. The measured noise on a functioning channel will decrease once it is biased above its depletion voltage, since its capacitance will decrease: unbonded strips or faulty ASIC channels will not display this dependence. However, it was found that the tuning of the selection was highly detector and condition sensitive and hence this method of faulty channel identification is less accurate for repeated semi-automatic analysis than those discussed below.

The cluster finding efficiency analysis can also be used to determine the number of dead channels in the detector. A track is extrapolated to the detector and clusters searched for in the channels around the intercept point. A channel is identified as dead if tracks extrapolated to this strip show four times more missed clusters than the mean of the 30

Table 1: Fraction of faulty strips classified as dead or noisy. The results are obtained from the methods used at production, occupancy spectrum studies, and a cluster finding efficiency analysis. Values are given at the time of production or start of operations in 2010, at the end of 2011, and at the end of 2012.

Delivered Int. Luminosity	$0 \text{ fb}^{-1}$	$1.2 \text{ fb}^{-1}$	$3.3 \text{ fb}^{-1}$
Dead Strips			
Production Tests	0.6%	–	–
Occupancy	0.7%	0.7%	0.6%
Cluster Finding Efficiency	0.8%	1.1%	–
Noisy Strips			
Production Tests	0.02%	–	–
Occupancy	0.01%	0.02%	0.02%

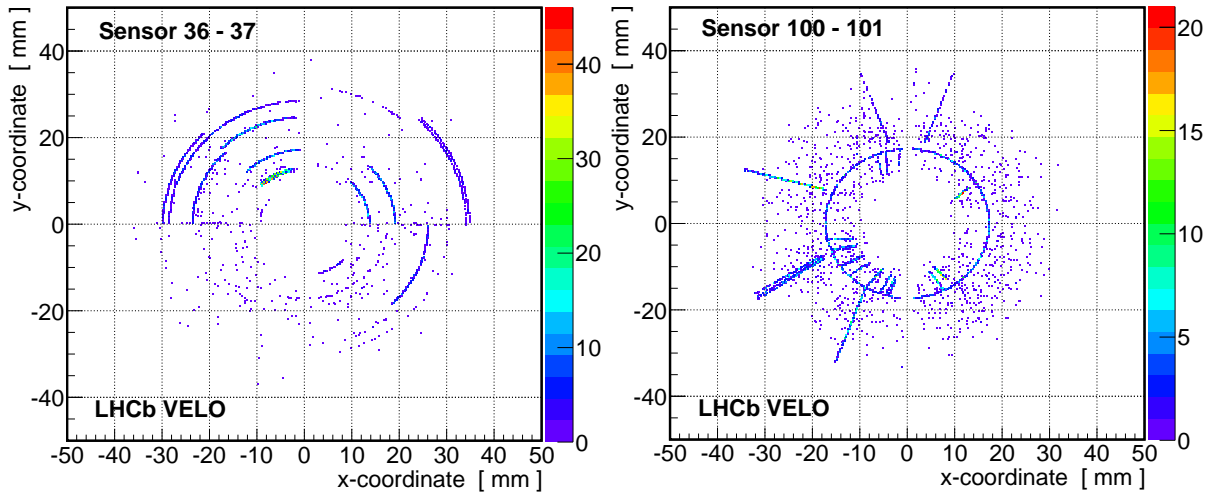


Figure 22: The intercept position of an extrapolated track when a cluster is not found for two example  $R$  (left) and  $\Phi$  (right) sensors. The bad channels are clearly visible.

nearest neighbours. Examples of the locations of strips in which clusters are not found are shown in Fig. 22, which shows the boundary region on the  $\Phi$  sensor between the inner and outer strips and the location of bad strips. This method identifies 89% of the channels found in the dead channel list made at production. Only 0.8% of channels were identified as dead at the start of operations by the cluster finding analysis method. At the end of 2011, after two years of operation and a delivered fluence of  $1.2 \text{ fb}^{-1}$ , the fraction had increased to 1.1% of channels.

Two classes of faulty strips, dead and noisy, are also identified through the analysis of the channel occupancy spectra (see Sect 4.3). Faulty channels are usually masked in the FPGA data processing algorithms, and hence would not show up in the occupancy spectra. Therefore, the analysis is performed using NZS data and emulating the data processing,

but without the faulty channel mask applied. Channels with less than 10% of the average occupancy are identified as dead, and those with greater than three times the average occupancy as noisy. The results are compared with those found at production and with the cluster finding efficiency method in Table 1, and seen to be in good agreement. The level of dead and noisy strips is shown to have remained at a low level throughout the operations.

## 4.6 Radiation damage studies

The proximity of the silicon sensors to the LHC beam results in a high particle fluence of up to  $5 \times 10^{13}$  1 MeV neutron equivalents /  $\text{cm}^2$  ( $n_{\text{eq}}$ ) per  $\text{fb}^{-1}$  of delivered integrated luminosity for the most irradiated sensor regions, varying by approximately a factor of two as a function of the position of the sensors along  $z$ . The VELO geometry, with the sensors placed perpendicular to the beam, gives rise to a highly non-uniform radiation dose across the sensors with the fluence falling off with radius  $r$  as approximately  $r^{-1.9}$ . The estimated fluence is obtained from the LHCb simulation and using measured values of displacement damage in silicon. Particle irradiation gives rise to both bulk and surface damage effects in the silicon. The bulk radiation damage is primarily caused by the displacement of atoms in the silicon sensors from their lattice sites, and induces changes in the leakage current and effective doping concentration of the material. Consequently, radiation damage monitoring was put in place from the start of operations. The leakage currents, noise and charge collection efficiency (CCE) of the sensors are studied regularly, with dedicated data taking scan procedures having been developed. Detailed studies of radiation damage in the VELO based on 2010 and 2011 data taking have been reported in Ref. [30]. Further results, based on the 2012 and 2013 data taking periods, are summarised here.

### 4.6.1 Current measurements

Sensor currents are studied as a function of both voltage and temperature. Current-voltage scans are taken with an automated procedure on a weekly basis. The shapes are analysed to look for signs of gradient changes that could indicate the onset of breakdown, and the values at the operational voltage of 150 V are compared to the expected currents. Current-temperature scans are taken a few times a year by controlling the temperature of the cooling system. The current-temperature scans allow the surface and bulk current components to be measured separately. More details of these studies are available in Refs. [31, 32].

The expected increase in the bulk current in each sensor due to radiation damage is calculated using the predicted fluences and the measured temperature history of the sensor and the relation [33]

$$\Delta I = \alpha \phi V_{\text{Si}},$$

where  $\alpha$  is the annealing parameter in units of A/cm, which depends on the temperature history,  $\phi$  is the fluence in particles per  $\text{cm}^2$  and  $V_{\text{Si}}$  is the silicon volume in  $\text{cm}^3$ . The



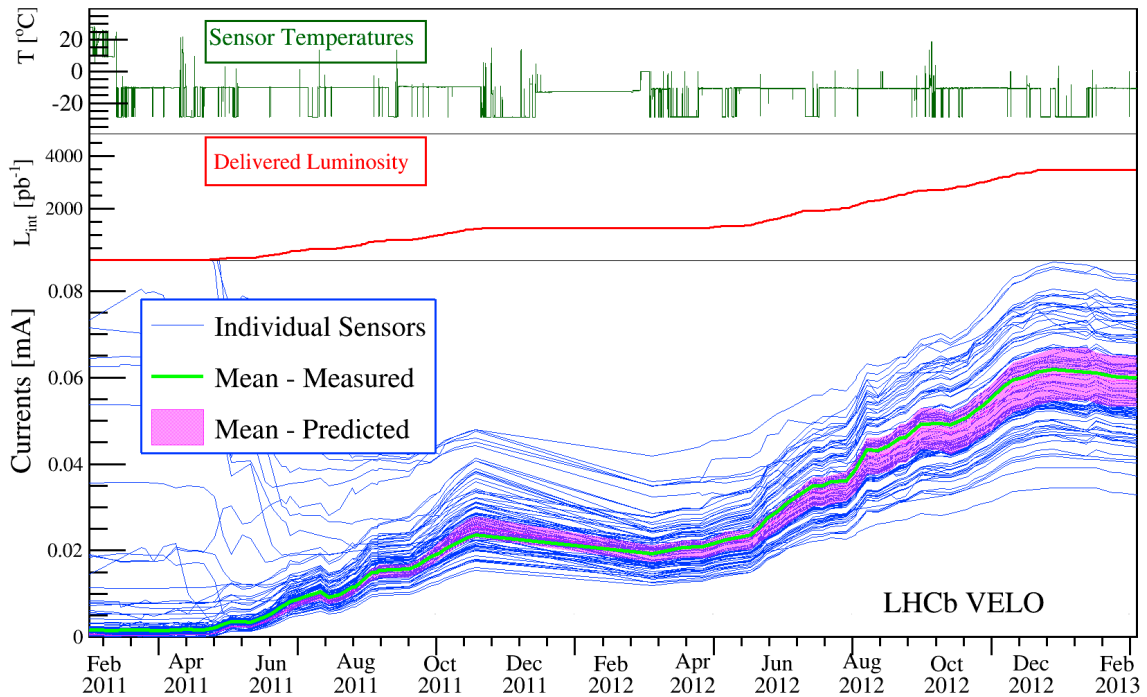


Figure 23: Currents measured for each sensor as a function of time (bottom). The integrated luminosity delivered to LHCb and the average sensor temperature is shown over the same time scale (middle and top). Increases in the delivered luminosity are matched by increases in the sensor currents. The evolution of the mean measured current agrees well with the prediction from simulation. The mean measured value excludes sensors that are surface-current dominated.

evolution of the observed currents in the sensors with delivered integrated luminosity are in good agreement with the expectation (see Fig. 23).

#### 4.6.2 Effective doping concentration

The  $n$ -bulk sensors undergo space-charge sign inversion under irradiation, and hence their depletion voltage initially reduces with irradiation. This continues until type inversion occurs, after which it increases with further irradiation. In order for the charge collection efficiency of the sensors to remain reasonably high, the sensors must be close-to or fully depleted during operation. As all of the VELO sensors are operated at a constant voltage over long periods, monitoring the sensor depletion voltages is a useful experimental technique for ensuring that the CCE for a particular sensor does not decrease significantly due to the sensor being under-depleted. In practice, this is achieved by monitoring the effective depletion voltage (EDV), which is derived using the following method. Here we report results for the  $n$ -type sensors, but note that one  $p$ -type module is also installed in the VELO and is studied in Ref. [30].

Sensors are grouped into a 1-in-5 pattern, where four of the sensors are operated at the nominal operation voltage (150 V throughout 2010–2013) whilst a single sensor, referred to as the test sensor, has a range of bias voltages applied to it. Using only the sensors at the nominal operation voltage, a track is then fitted and extrapolated to the test sensor, where the amount of collected charge at the intercept is determined. The distribution of collected charge arising from repeating this process for many tracks is fitted with a Landau distribution convolved with a Gaussian distribution to obtain the MPV of the Landau distribution. The EDV is then determined as the voltage at which the MPV of the charge distribution is equal to 80% of the MPV obtained at the maximum test voltage (currently 200 V). This value of 80% provides good agreement between the depletion voltage measured from this method prior to irradiation and that obtained from the capacitance-voltage measurements performed on the sensors at production. It also represents a voltage above which the sensors must be operated to ensure significant signal charge is extracted. This process then repeats via an automated procedure for a range of patterns such that all of the sensors are tested. As this procedure requires beam time that would otherwise be used for physics data taking, it is currently only performed around three times per year.

Figure 24 shows the measured EDV values using all the VELO sensors, and dividing them into radial regions with reasonably constant fluence. The delivered integrated luminosity at each CCE scan has been combined with the expected fluence per  $\text{fb}^{-1}$  to give the fluence for each radial region of each sensor. The sensors exhibit an overall decrease in EDV with fluence followed by an increase in EDV until the most recent CCE scan (after a delivered integrated luminosity of  $3.4 \text{ fb}^{-1}$ ). As a result of the radiation damage that had occurred by the start of 2013, many of the sensors now have EDVs significantly higher than before irradiation. On average, type inversion of the silicon occurs around  $20 \times 10^{12} \text{ n}_{\text{eq}}$ , after which the EDV increases linearly with fluence. This behaviour can therefore be used to predict the operational voltages required to give maximal CCE for a given fluence and hence a delivered integrated luminosity. It can also be noted that a minimum EDV of  $\sim 20 \text{ V}$  is observed for all sensors, this is assumed to be a result of the finite integration time of the front-end electronics.

### 4.6.3 Charge loss to second metal layer

The cluster finding efficiency in the sensors is studied using the same technique of track extrapolation as that used to study the CCE (see Sect. 4.6.2). These studies have shown an unexpected radiation induced charge loss due to the presence of the second metal layer on the sensors. The second metal layer on the sensors is used to route signals from inner strips to the outer radius of the sensor. Particles that pass close to a second metal layer trace, but away from the shielding effect of the first metal layer on the strip, have a reduced charge collected on this strip and additionally induce charge on the second metal layer. This gives rise to a reduction in cluster finding efficiency on this strip, and additional noise clusters located on the strip connected to the second metal layer track. This degradation has been observed to continue throughout the 2012 data taking period,

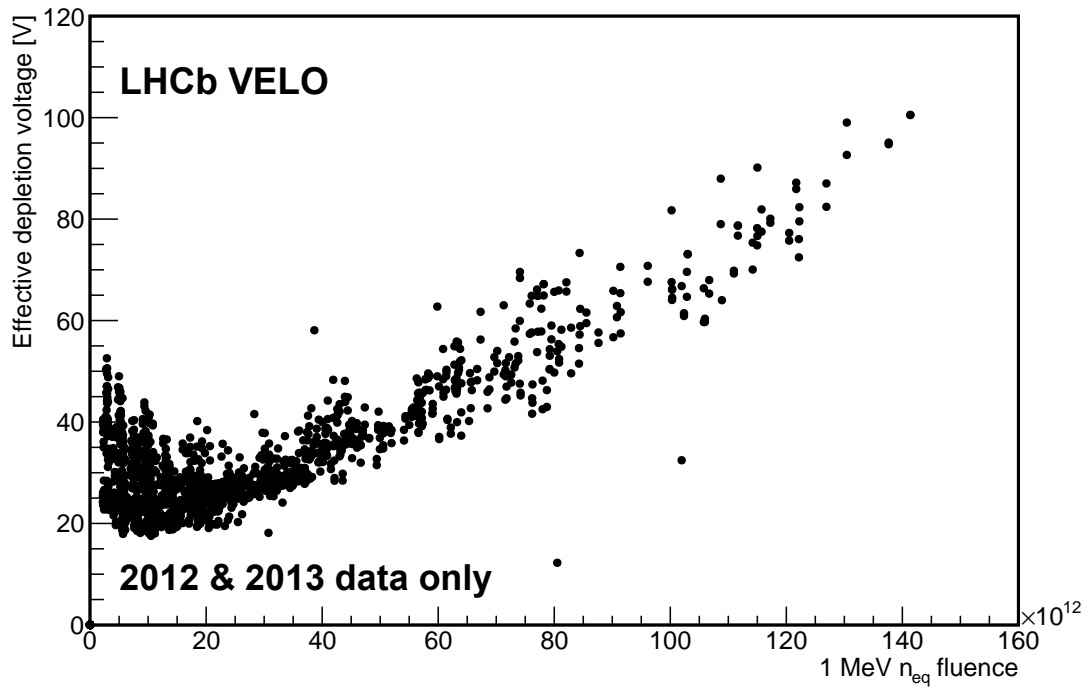


Figure 24: The effective depletion voltage versus fluence for all VELO sensors up to  $3.4 \text{ fb}^{-1}$  delivered integrated luminosity.

although there is some evidence to suggest the rate of change with fluence is decreasing. Currently studies of the VELO tracking efficiency show no degradation associated with this effect within the errors of  $\pm 0.3\%$ . This effect is discussed in detail in Ref. [30].

## 5 Physics performance

The performance of the VELO on more directly physics analysis related parameters is reviewed in this section. The performance of the pattern recognition, track reconstruction and the alignment of the detector are discussed. The impact parameter, primary vertex (PV) resolution and decay time resolution of the detector are then presented.

### 5.1 Pattern recognition and tracking

Obtaining a high efficiency for reconstructing the trajectories of charged particles is particularly important for the analysis of many-body final states since the selection efficiency scales with the track finding efficiency to the power of the number of tracks. An accurate knowledge of the tracking efficiency is also important in many other physics analyses, especially those that aim to measure a production cross-section or a branching fraction. The track finding algorithms in LHCb start with a search in the VELO detector for straight lines. These tracks are then combined with hits in the tracking stations to produce the “long” tracks that are used for most physics analyses. The track fit is performed using a Kalman fit. In the trigger a simplified model of the detector material and a single direction Kalman fit are used in order to reduce CPU consumption. A full bi-directional Kalman fit is performed offline using a detailed model of the detector material.

The VELO pattern recognition algorithm requires a minimum of three  $R$  sensor and three  $\Phi$  sensor clusters to reconstruct a trajectory. The basic algorithm collects sets of  $R$  clusters consistent with being on a straight line from the interaction point, then looks for a set of compatible  $\Phi$  sensor clusters to confirm the trajectory. The alternating stereo angles of the  $\Phi$  sensor strips resolves the stereo ambiguities when combining the  $R$  and  $\Phi$  sensor clusters. A second pass is made combining the unused clusters to find tracks not from the interaction region. The number of clusters on a VELO track ranges from six (the minimum requirement is three on  $R$  and three on  $\Phi$  sensors) up to the full 42, with an average of 11. An additional algorithm, that only runs when the detector is closing, makes 3D space points from the  $R$  and  $\Phi$  sensor clusters in a module and forms tracks from these having no assumptions about the track directions.

The efficiency of the track reconstruction in the VELO has been measured using a tag-and-probe method. Samples of  $J/\psi$  decays into two muons are used where the track of one of the muons is fully reconstructed (tag-muon), while the other muon is only partially reconstructed using hits in the other tracking stations (probe-muon). The momenta of the tag- and probe-muon are used to reconstruct the  $J/\psi$  candidate mass and hence confirm the selection. It is required that the trigger has not selected the event based on the probe muon track to prevent any potential trigger bias. The VELO tracking efficiency is obtained by matching the partially reconstructed probe muon to a long track (which has a VELO track segment).

The measured VELO tracking efficiency for long tracks is shown in Fig. 25 for data and simulation, and is typically 98% or higher in the data. The simulation is weighted by the

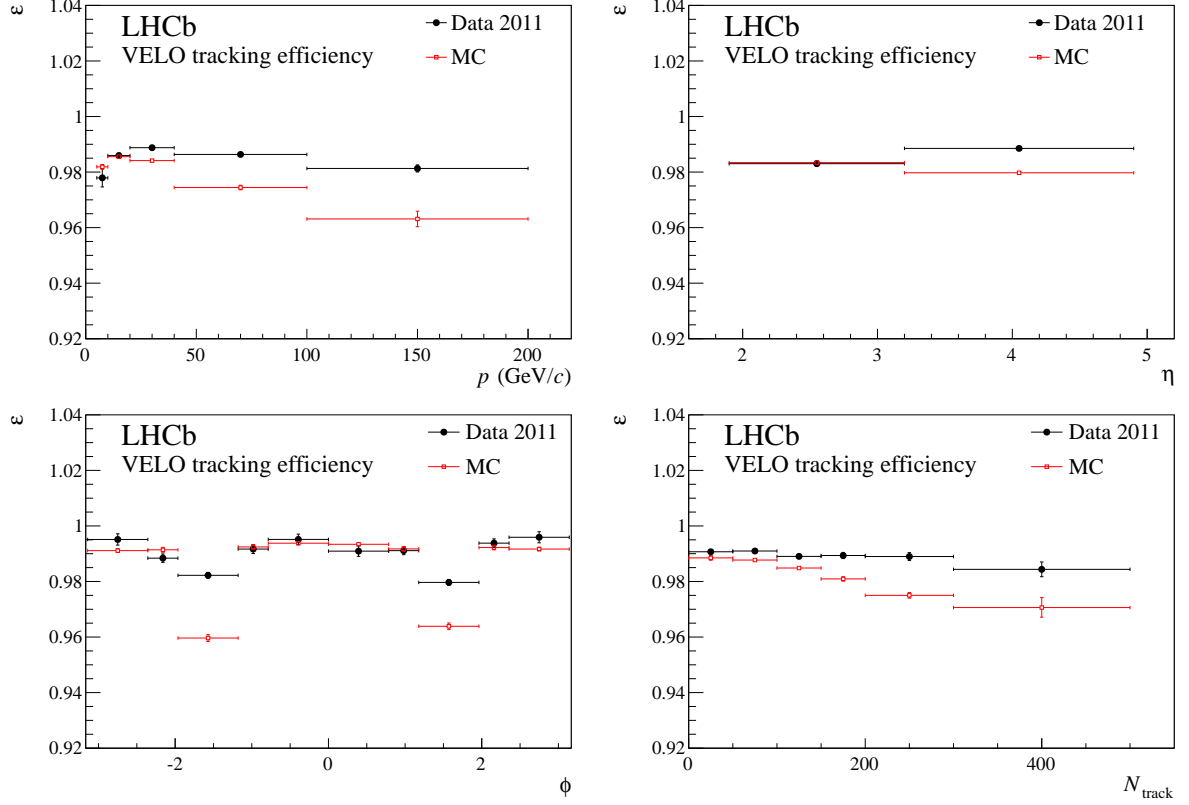


Figure 25: Tracking efficiency for the 2011 data and simulation for the VELO as a function of the momentum,  $p$  (top left), the pseudorapidity,  $\eta$  (top right), the azimuthal angle  $\phi$  (bottom left) and the total number of tracks in the event,  $N_{track}$  (bottom right). The simulation has been reweighted to the number of tracks observed in data for the  $p, \eta$  and  $\phi$  plots. The error bars indicate the statistical uncertainty.

number of tracks observed in the data. The efficiency for the VELO pattern recognition is weakly dependent on the multiplicity of the event, as the pattern recognition becomes more complex in a higher occupancy environment. The dips in efficiency at  $|\phi| \approx \pi/2$  are caused by the extra multiple scattering from the material of the RF foil in the vertical plane, see Fig 5 (left). The discrepancy between data and simulation in these bins is partially explained by the effect of assumptions made in the tracking: the beam is centred in the coordinate system in the simulation while it is offset by 0.4 mm in data; and the distance between the two halves when the system is fully closed differ at the  $150 \mu\text{m}$  level between data and simulation. The discrepancy is taken into account in physics analyses by applying a reweighting procedure that ensures data and simulation agreement, and a procedure for determining the systematic uncertainties due to this correction is also in place.

Another important measure of the tracking performance is the number of poor quality

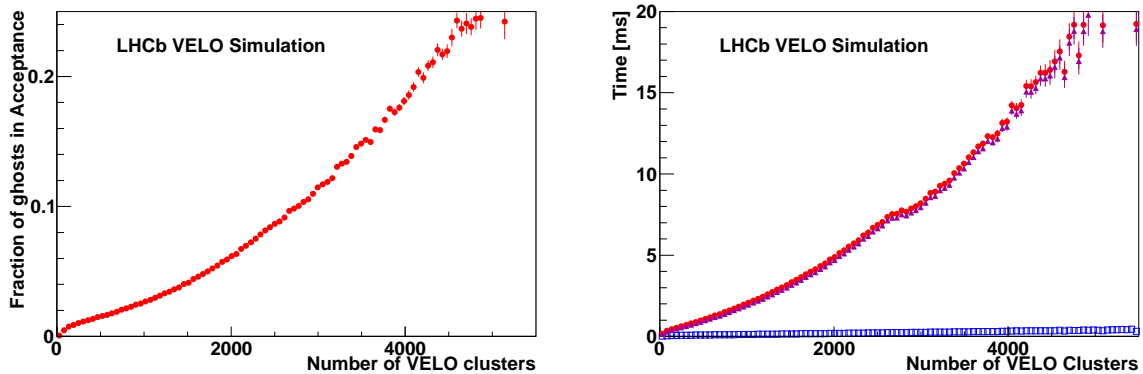


Figure 26: (left) Fraction of ghost tracks versus number of VELO clusters in simulation. (right) VELO pattern recognition timing versus number of clusters, the pattern recognition alone (magenta triangles), the raw data decoding (blue squares) and the combined (red circles) timings are shown. The times are scaled to a 2.8 GHz Xeon processor.

or “ghost” tracks that are produced. Defining a ghost track as one in which less than 70% of the VELO clusters on the track are from the same simulated particle, the fraction of ghost tracks is shown in Fig. 26 (left) as a function of the total number of VELO clusters. These tracks become more frequent as the detector occupancy rises, with typical occupancies being 0.5% for randomly triggered events and 1% for HLT triggered events (see Sect. 4.3).

The CPU resources consumed by the VELO tracking in the high level trigger are substantial and the algorithms have been optimised for speed. For example, to minimise the time taken in decoding the clusters, the 3-bit cluster centre position computed in the TELL1 FPGAs is used (see Sect. 3.3). The time taken for the decoding and pattern recognition algorithms is shown in Fig. 26 (right).

## 5.2 Alignment

The VELO has extremely stringent alignment requirements to ensure that the intrinsic hit resolution of the detector (see Sect. 4.2) and the impact parameter and decay time resolution (see below) of the experiment are not adversely affected. Furthermore, as described in Sect. 2.5, the VELO halves are inserted and centred around the beams in each LHC fill. Consequently the high level trigger requires an immediate update of the alignment parameters. These parameters are also required for the offline reconstruction. The alignment of the detector is thus separated into two elements: the underlying system alignment, and the updates required in each fill.

The underlying alignment of the VELO relies on three components: the precise construction and assembly of the detector, the mechanical and optical survey of each part of the detector, and the software alignment of the system using tracks. The updates for

each fill are then added to this: mechanical measurements of the position to which the detector is closed are used to determine these.

### 5.2.1 Optical and mechanical measurements

Each component of the detector was surveyed at the various stages of the assembly using a smart-scope for the individual modules, and a coordinate measuring machine with optical and touch probe heads for the modules and for each half of the assembled system. The relative position of the  $\Phi$  sensor with respect to the  $R$  sensor in each module was measured with an accuracy of about  $3\ \mu\text{m}$  for the  $x$  and  $y$  translation and with an accuracy of about  $20\ \mu\text{rad}$  for rotations around the  $x$  and  $y$  axis. The relative module positions within each half of the detector were measured with a precision of about  $10\ \mu\text{m}$  for the translations along  $x$  and  $y$ . Measurements of the mounting frame were made with a coordinate measuring machine during production, and then prior to, and after, installation measurements were made using photogrammetry, theodolites, mechanical gauges and levelling instruments. The position of the two VELO halves was determined with an accuracy of  $100\ \mu\text{m}$  for the translations and  $100\ \mu\text{rad}$  for the rotations. These survey measurements are used as a starting point for the track-based software alignment, and remain important for the final alignment quality as some degrees of freedom (see below) are difficult to align with tracks.

### 5.2.2 Track-based alignment methods

The track-based alignment relies on minimising the residuals between the fitted tracks and the measured cluster positions. The alignment can be considered in terms of three different stages:

1. the relative alignment of each  $\Phi$  sensor with respect to the  $R$  sensor in the same module. This allows the  $x$  and  $y$  translations of the sensors to be determined;
2. the relative alignment of the modules within each VELO half. This alignment is primarily sensitive to the  $x$  and  $y$  translations of the modules and their rotations around the  $z$  axis. Only the  $\Phi$  sensors are sensitive to this rotation due to the strip geometry and hence this rotation must be determined at the module level. The misalignment due to the other three degrees of freedom (the  $z$  translation and the rotations around the  $x$  and  $y$  axis) cause second order effects to which sensitivity can only be obtained with  $R$  sensors from using a large data sample with a wide range of track angles;
3. the relative alignment of one VELO half with respect to the other half. The PV position can be used as a constraint since tracks reconstructed in each half originate from this common point. This method is sensitive to the  $x$ ,  $y$  and  $z$  translations and the rotations around the  $x$  and  $y$  axis. In addition, tracks that cross both halves of the detector are used. There is a small overlap between the sensors in the left and right halves of the VELO when the detector is fully closed, and tracks that traverse the VELO in this overlap region are particularly important. The alignment using

these tracks is mainly sensitive to the misalignment of  $x$  and  $y$  translations and the rotation around the  $z$  axis.

Two methods were developed and used for performing the track-based software alignment. The first method [34, 35] performs the  $\Phi$  sensor alignment by fitting an analytical form to the residuals as a function of  $\phi$ , and performs the remaining alignment stages using a matrix inversion method, based on Millepede [36], which performs a  $\chi^2$  minimisation that depends upon both the track and alignment parameters. This alignment method is fast but the implementation fits straight line tracks in the VELO. The second method uses a global  $\chi^2$  minimisation based on Kalman track fit residuals [25]. This method uses an iterative procedure, that could be time consuming in the case of a large misalignment. However, the Kalman filter fit takes into account the corrections for multiple scattering, energy loss effects and the weak magnetic field in the VELO region. The results from both methods are in agreement [14].

The alignment is performed using a specially selected data sample which improves the sensitivity to all degrees of freedom and better constrains the upstream and downstream of the PV regions of the VELO. This sample includes a mixture of tracks from collisions with a wide range of angles, and tracks from beam-gas interactions. The beam-gas interactions are roughly parallel with the beam-axis, giving tracks that cross many modules.

Correlated module misalignments which are poorly constrained in the track-based alignment, known as weak modes, can bias physics quantities like the impact parameter or the invariant mass. The most important weak mode in the VELO is the twist of the modules around the  $z$ -axis. This misalignment can distort the impact parameter measurement by several tens of microns as a function of the azimuthal direction of the track. The effect is limited by using the alignment track sample with a range of track types, and by applying constraints in the alignment procedure from the survey measurements.

### 5.2.3 Mechanical measurement of closing

The VELO halves are moved independently horizontally ( $x$ ) and together vertically ( $y$ ) during the closing procedure and the motion is measured to an accuracy of a few  $\mu\text{m}$  with mechanical position sensors. These measure the revolutions of the spindle that controls the displacement. The position of the two VELO halves is updated for each fill using these mechanical system measurements in  $x$  and  $y$  by adding these changes to the underlying system alignment.

Performing the track-based alignment of the VELO halves using data collected at different opening positions (distance between the two halves of 0,  $\pm 5$  mm,  $\pm 10$  mm,  $\pm 29$  mm) allows a calibration of the motion system measurements to be performed. This shows a calibration accuracy of 0.6% of the motion system along the  $x$  direction is achieved.

### 5.2.4 Alignment performance

The track-based alignment results are in good agreement with the lower precision survey results, within the uncertainties, apart from the effect due to the change in temperature



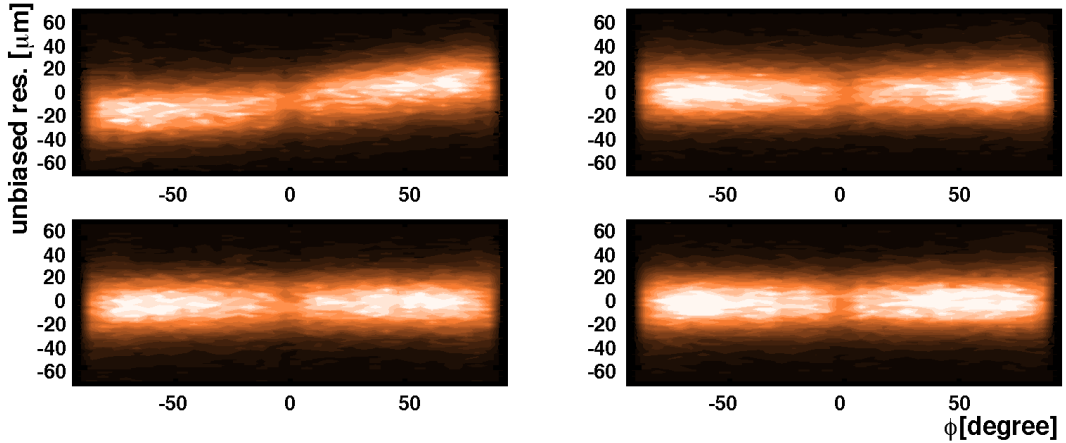


Figure 27: Example unbiased sensor residuals as a function of the  $\phi$  coordinate using only the survey information (left) and using the track-based software alignment (right). Results are given for two different example sensors. (top) A significant improvement in the residuals is seen in this sensor with the track-based alignment. (bottom) In this sensor the alignment quality using the survey information is already good.

of the system. The system was surveyed at room temperature, but is normally operated with the cooling system operated at  $-30^{\circ}\text{C}$ . Comparing track-based alignments performed with the cooling temperature set to  $+8^{\circ}\text{C}$  and  $-30^{\circ}\text{C}$  a change of distance between the two halves of about  $170\ \mu\text{m}$  was measured. Laboratory measurements were also made by heating individual modules and an expansion of approximately  $1\ \mu\text{m}$  per degree along the  $x$  direction of the carbon fibre that supports the modules was found. Hence, even when using materials with a low coefficient of thermal expansion it is important to control temperature changes when aiming for  $\mu\text{m}$  level precision. This is achieved in the VELO by maintaining the mounting base plate of each VELO half at  $20^{\circ}\text{C}$  and operating with a stable cooling system temperature.

The improvement obtained after the track-based alignment procedure over the precision of the survey is illustrated in Fig. 27. The shapes of the residual distributions as a function of the azimuthal coordinate are characteristic of particular sensor misalignments. The precision obtained after the track-based alignment is better than the best hit resolution of the detector with an alignment at the few  $\mu\text{m}$  level obtained for the  $x$  and  $y$  module translations.

Fitting the position of the PV separately with tracks in the two halves of the VELO allows the misalignment between the two halves to be determined. This is shown in Fig. 28 over a period of four months of operation. The variation between runs shows the accuracy with which the position in each fill is measured. The excellent stability of the alignment of the system is also clear.

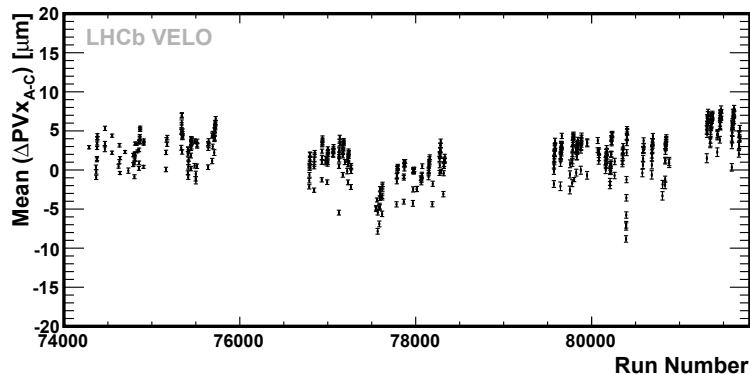


Figure 28: Misalignment between the two VELO halves in each run, evaluated by fitting the PV separately with tracks in the two halves of the VELO. The run numbers shown here span the period of the last four months of operations in 2010.

### 5.3 Primary vertex resolution

The accurate measurement of decay lifetimes is required for the primary physics aims of the LHCb experiment in CP violation and rare decay studies. Precise vertex reconstruction is therefore of fundamental importance, in order to resolve production and decay vertices.

The PV resolution is strongly correlated to the number of tracks  $N$  used to reconstruct the vertex. The analysis is performed on an event-by-event basis. The principle is to reconstruct the same PV twice, and to determine the difference between these two PV positions. This is achieved by splitting the track sample of each event into two and making vertices from each independent set of tracks. The method was verified in the simulation by comparing the reconstructed and generator level information.

The track splitting is done entirely at random, with no ordering of tracks and no requirement that the same number of tracks is put into each set. The vertex reconstruction algorithm is applied to each set of tracks. Vertices are ‘matched’ between the two sets by requiring that the difference in their  $z$  position is  $< 2$  mm. Then, if the number of tracks making a pair of matched vertices is the same, the residual is calculated. Repeating for many events yields a series of histograms of residuals in  $(x, y, z)$  for varying track multiplicity.

In practice, the number of tracks making a vertex ranges from 5 (the required minimum) to around 100. However, given the track splitting method roughly divides the total number of tracks in two, it is difficult to measure the resolution past 40 tracks. Each residual histogram is fitted with a Gaussian distribution. The resolution for each particular track multiplicity is calculated as the  $\sigma$  of the fitted Gaussian divided by  $\sqrt{2}$ , as there are two uncorrelated resolution contributions in each residual measurement.

The resolution is fitted with a function which parametrises it in terms of  $N$  as follows:

$$\sigma_{PV} = \frac{A}{\sqrt{N}} + C, \quad (1)$$

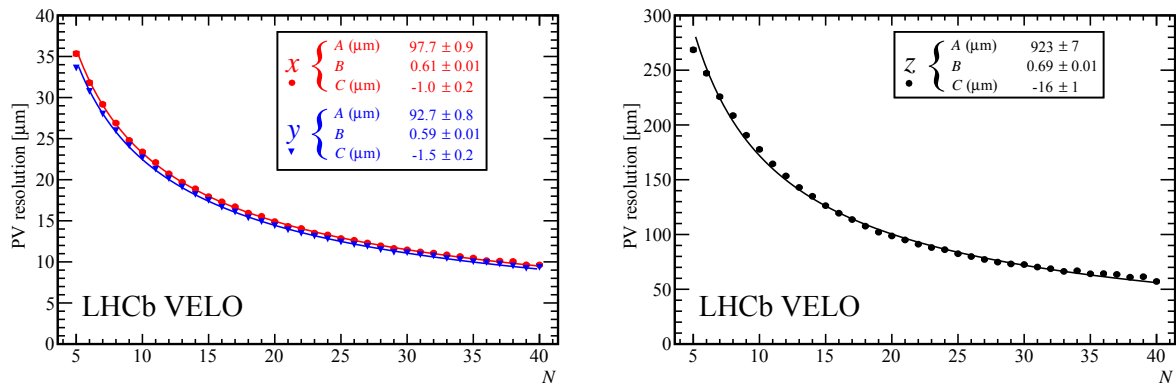


Figure 29: PV Resolution of events with exactly one PV in 2011 data as a function of track multiplicity. (left)  $x$  (red) and  $y$  (blue) resolution and (right)  $z$  resolution. The fit parameters  $A$ ,  $B$  and  $C$  for each coordinate are given.

where  $A, B, C$  are constants.

In 2011 data it was found that a 25-track vertex has a resolution in the transverse plane of  $13 \mu\text{m}$ , while the resolution in  $z$  is  $71 \mu\text{m}$ , as shown in Fig. 29. The 2011 simulation had a resolution approximately  $2 \mu\text{m}$  better than in the data. For data with an average number of visible proton-proton interactions per bunch crossing of around 1.3, the average number of tracks in a minimum bias event containing one PV is 55. The equivalent number in an event in which a candidate  $B$  decay has been reconstructed is 120. As the number of reconstructed PVs in the event increases, the resolution degrades. The rate of degradation is approximately 5–10% per additional vertex. The vertex resolution results for 2012 data are very similar.

The stability of the PV position has also been studied. In a single fill the PV position was found to move in  $x$  and  $y$  by not more than  $4 \mu\text{m}$  and  $2 \mu\text{m}$  respectively. Based on analysing a three-month data sample from 2012, the PV position in the LHCb coordinate system was found to move by a maximum of  $50 \mu\text{m}$  (RMS= $16 \mu\text{m}$ ). The VELO is centred around the beam with a maximum variation of  $20 \mu\text{m}$  in  $x$  and  $40 \mu\text{m}$  in  $y$ . For a conservative estimate we apply a safety factor of two to the total variation, and determine that the beam stability with respect to the VELO is better than  $100 \mu\text{m}$ .

## 5.4 Impact parameter resolution

The impact parameter (IP) of a track is defined as the distance between the track and the PV at the track's point of closest approach to the PV. The  $B$  and  $D$  mesons studied in many LHCb analyses are long lived particles and hence their decay vertex is generally displaced from the PV. The tracks made by particles coming from the decay of long lived particles therefore tend to have larger IPs than those made by particles produced at the PV. Consequently, cuts on the IP are very effective at excluding prompt backgrounds, and maximising the signal content of a data set. It is thus of great importance for an

experiment like LHCb to be able to measure IPs to a high precision, and to have a good understanding of the effects contributing to the resolution of IP measurements.

The IP resolution is governed by three main factors: multiple scattering of particles by the detector material; the resolution on the position of hits in the detector from which tracks are reconstructed; and the distance it is required to extrapolate a track from its first hit in the detector to the PV. An approximate analytical expression can be derived [12],

$$\sigma_{IP}^2 = \left( \frac{0.0136}{p_T} \sqrt{x/X_0} [1 + 0.038 \ln(x/X_0)] \right)^2 r_1^2 + \frac{\Delta_{02}^2 \sigma_1^2 + \Delta_{01}^2 \sigma_2^2}{(\Delta_{02} - \Delta_{01})^2}, \quad (2)$$

where the first term is due to multiple scattering and the second term due to the detector resolution. The particle has a transverse momentum  $p_T$  and it passes through a piece of material, of thickness  $x$ , and with radiation length  $X_0$ . The track is extrapolated over a distance  $\Delta_{01}$  between the first hit on a track and the PV, and the distance from the PV to the second hit is  $\Delta_{02}$ . The resolution of the first and second hits on the track are  $\sigma_1$  and  $\sigma_2$ . This expression applies to a 1D IP measurement. Parametrising the resolution in the plane perpendicular to the beam,  $IP_x$  and  $IP_y$ , as a function of  $1/p_T$  one expects identical, roughly linear distributions with an  $x$  or  $y$ -intercept dependent on the detector resolution, and a gradient proportional to the material budget. In 3D geometry an IP has two degrees of freedom: three as it is a distance in 3D space, minus one from the requirement of being calculated at the point of closest approach to the PV. Due to the forward geometry of LHCb the  $z$  component is negligible, and the IP measurement in 3D space is thus simply the sum in quadrature of its  $x$  and  $y$  components. The mean offset of such a measurement from its true value is given by the resolution on the 1D components multiplied by  $\sqrt{\pi/2}$ .

The vast majority of tracks reconstructed at LHCb are made by particles produced promptly at the PV. The measured IP of such tracks is non-zero only due to the measurement resolution. Thus, the IP resolution can be measured by examining the width of the  $IP_x$  and  $IP_y$  distributions for all tracks. To do this, only good quality long tracks from events with only one reconstructed PV are used. The PV is required to have at least 25 tracks included in its fit to minimise the contribution of the vertex resolution to the measured IP. Furthermore, the PV is refitted excluding each track in turn before its IP is calculated so the track has no influence on the PV position. The  $IP_x$  and  $IP_y$  are then plotted in bins of the variable of interest, such as  $1/p_T$ , and a fit of a Gaussian function performed in each bin. The width of the fitted Gaussian is taken as the resolution.

Figure 30 shows plots of the IP resolution versus momentum and  $1/p_T$ . The resolution of  $IP_x$  and  $IP_y$  is almost identical. They are asymptotic at high  $p_T$ , tending to  $\sim 12 \mu\text{m}$ , and depend roughly linearly on  $1/p_T$ . The performance of the VELO in this respect is excellent, achieving IP resolutions of  $< 35 \mu\text{m}$  for particles with  $p_T > 1 \text{ GeV}/c$ .

The distribution of material in the VELO is non-uniform, and this also affects IP resolutions. The excellent agreement with simulation shown in Fig. 30 was only obtained after careful study of the material distribution in the RF foil. In the region in which the two halves of the VELO overlap the two sides of the RF foil also overlap, greatly increasing the material density. This can be seen by measuring the IP resolution in bins

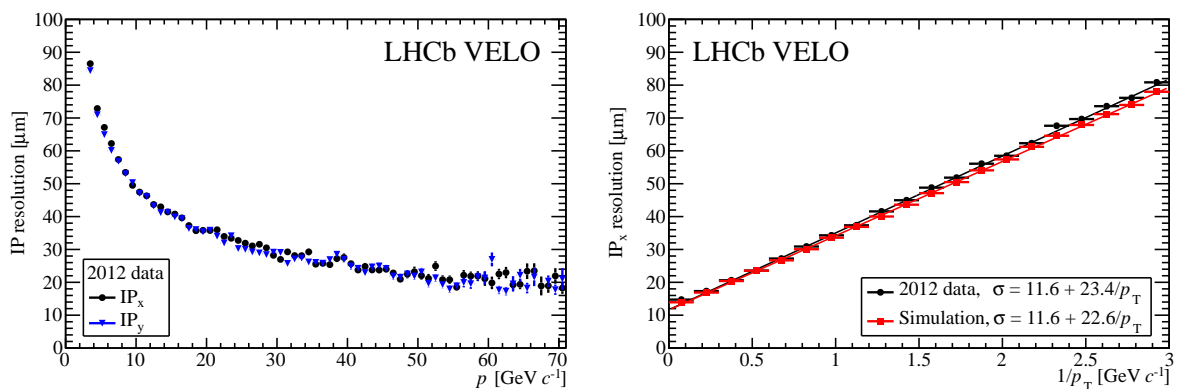


Figure 30:  $IP_x$  and  $IP_y$  resolution as a function of momentum (left) and  $IP_x$  as a function of  $1/p_T$  and compared with simulation (right). Determined with 2012 data.

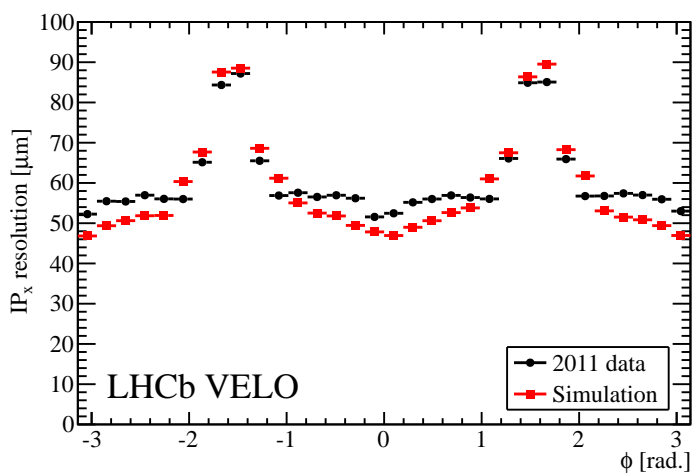


Figure 31:  $IP_x$  resolution as a function of azimuthal angle  $\phi$ , measured on 2011 data and compared to simulation.

of the azimuthal angle  $\phi$ , as is shown in Fig. 31. The increase in material is reflected in the increase in IP resolution about  $\phi = \pm\pi/2$ , *i.e.* in the overlap region.

Thus, it can be seen that the VELO provides accurate IP measurements on which the LHCb physics programme relies for the rejection of prompt backgrounds to long-lived heavy flavour hadron decays. The IP resolution behaves as expected, with a roughly linear dependence on  $1/p_T$ , and a clear dependence on both the hit resolution and the distribution of material.

## 5.5 Decay time resolution

The reconstructed decay time of strange, charm and beauty hadrons is used in offline event selections and in precise measurements of lifetimes. However, the most stringent demands on the decay time resolution stem from the requirement to resolve the fast oscillations induced by  $B_s^0-\bar{B}_s^0$  mixing. Consequently, we illustrate the performance of the VELO with an analysis of the decay time resolution of  $B_s^0 \rightarrow J/\psi \phi$  decays.

The reconstructed decay time in the rest frame of the decaying particle can be expressed in terms of the reconstructed decay length  $l$ , momentum  $p$  and mass  $m$  of the particle in the LHCb frame as

$$t = \frac{m l}{p}. \quad (3)$$

The decay time is computed with a vertex fit that constrains the decaying particle to originate from the PV. The decay time uncertainty is a function of the actual decay time. For small decay times it is dominated by the resolution on the decay length  $l$ , which in turn is dominated by the secondary vertex resolution of the VELO. For large decay times, it is dominated by the momentum, which is mostly determined by the tracking stations before and after the LHCb magnet. The two contributions are approximately equal at several times the  $B$  hadron lifetime. Therefore, the momentum resolution plays only a small role.

Time dependent  $CP$  violation effects are measured as the amplitude of an oscillation in the  $B$  decay time distribution. The size of the observed amplitude is damped by a dilution factor from the finite decay time resolution. For a resolution function that is a single Gaussian function with RMS  $\sigma_t$ , the dilution is

$$D = \exp \left[ -\frac{1}{2} \Delta m^2 \sigma_t^2 \right], \quad (4)$$

where  $\Delta m$  is the mixing frequency.

The sensitivity to the oscillation amplitude is proportional to the dilution. Therefore, for optimal sensitivity the dilution must be as close to unity as possible. However, even more important is the understanding of the dilution itself, since a bias in the estimated dilution leads to a bias in the measurement of a  $CP$  violating effect.

The decay time resolution depends on the topology of the decay and is calibrated for each final state on data. The calibration method uses prompt combinations that fake signal candidates. Ignoring the small contribution from signal candidates and long-lived background, the shape of the prompt peak is determined only by the resolution function. Figure 32 (left) shows the decay time distribution for fake  $B_s^0 \rightarrow J/\psi \phi \rightarrow \mu^+ \mu^- K^+ K^-$  decays in data and simulation. The  $B_s^0 \rightarrow J/\psi \phi$  candidate selection is described in Ref. [8]. The contribution from signal decays (which would result in a tail on the right of the distribution) is removed. The RMS values quoted in the figure are computed using events with negative decay time or decay length only, to reduce the sensitivity to a small contribution from other  $B \rightarrow J/\psi X$  decays. For a mixing frequency of  $17.7 \text{ ps}^{-1}$ , the decay time resolution corresponds to a dilution of about 0.7.

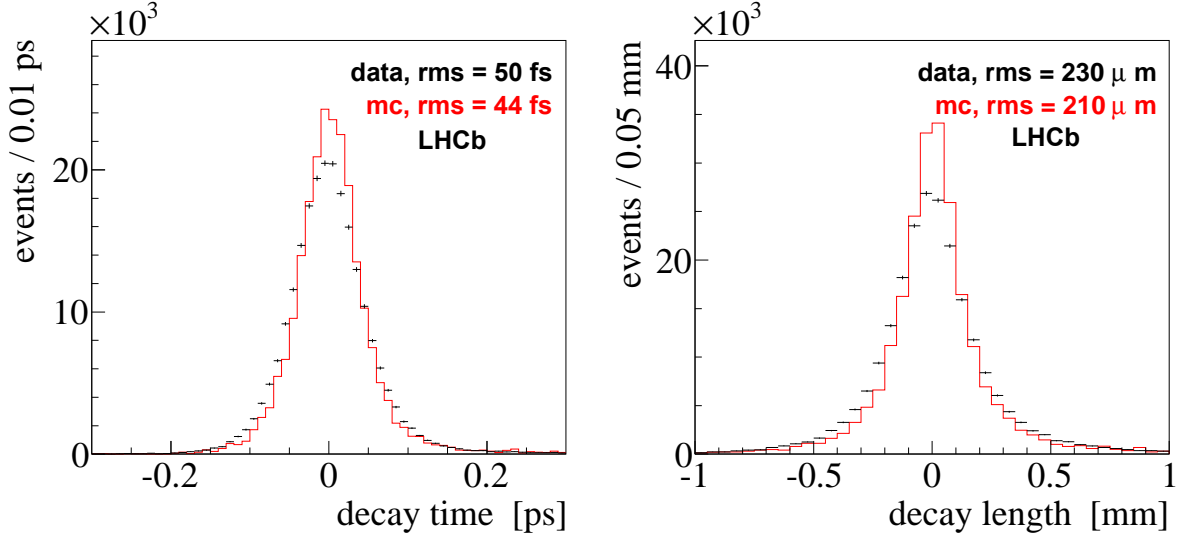


Figure 32: Decay time (left) and decay length (right) distribution for fake, prompt  $B_s^0 \rightarrow J/\psi \phi \rightarrow \mu^+ \mu^- K^+ K^-$  candidates in 2011 data (black points) and simulation (solid red histogram). Only events with a single PV are used. The simulated data are generated inclusive  $J/\psi$  events from which signal  $B_s^0 \rightarrow J/\psi \phi$  are removed. In the data contributions from non- $J/\psi$  di-muon combinations and from true  $B_s^0 \rightarrow J/\psi \phi$  are subtracted using the *sPlot* technique [37].

The resolution in both decay time and decay length is about 10% worse in 2011 data than in the corresponding simulated events. Note that the decay time resolution is more Gaussian shaped than the decay length resolution. This is largely because, for a fixed opening angle resolution, the decay length resolution is proportional to the momentum. This momentum dependence largely cancels in the decay time.

This effect is illustrated in Fig. 33 (left) which shows the resolution as a function of the (fake)  $B$  candidate momentum, where a mixing frequency of  $17.7 \text{ ps}^{-1}$  and Eqn. 4 have been used to obtain the decay time resolution. Only events with  $t < 0$  were used in order to reduce the sensitivity from remaining long-lived candidates. This procedure gives a resolution that is most relevant for the time-dependent  $CP$  violation measurement in  $B_s^0$  decays.

Finally, Fig. 33 (right) shows the resolution as a function of the per-event estimated uncertainty in the decay time. The latter is computed with the same vertex fit that computes the decay time itself. It is a non-trivial function of the track parameters and covariance matrices of the four final state particles in the decay. As expected, the resolution is a linear function of the estimated uncertainty. However, since track parameter uncertainties are not perfectly calibrated yet in the data, the slope is  $\sim 1.2$  rather than unity. The typical decay time resolution in LHCb is 50 fs, and this resolution plays a crucial role in the sensitivity of many LHCb physics measurements.

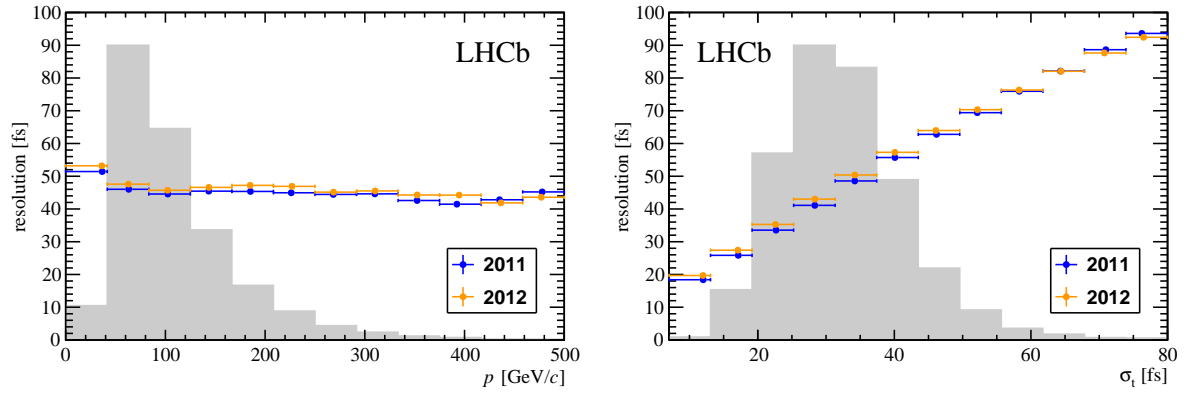


Figure 33: Decay time resolution (points) as a function of momentum (left) and as a function of the estimated decay time uncertainty (right) of fake, prompt  $B_s^0 \rightarrow J/\psi \phi \rightarrow \mu^+ \mu^- K^+ K^-$  candidates in data. Only events with a single PV are used. Contributions from non- $J/\psi$  di-muon combinations and from true  $B_s^0 \rightarrow J/\psi \phi$  are subtracted using the *sPlot* technique. The superimposed histogram shows the distribution of momentum (left) and estimated decay time uncertainty (right) on an arbitrary scale.



## 6 Conclusions

The performance of the LHCb VELO during its first years of operation has been described. The operational experience of key subsystems has been reviewed. The sensors have been successfully operated in a secondary vacuum at a pressure of  $2 \times 10^{-7}$  mbar, and cooled using a bi-phase CO<sub>2</sub> cooling system which has maintained the operating temperature of the sensors at  $(-7 \pm 2)^\circ\text{C}$ . The sensors are moved in 210 seconds from their fully retracted position to be centred 7 mm from the LHC beam for physics operation to an accuracy of better than 4  $\mu\text{m}$ . The average material budget of the detector for tracks in the LHCb acceptance is  $0.22 X_0$ .

The determination of the sampling time of the front-end pulse-shape and the digitisation time to maximise the signal, minimise spillover to the next and preceding event, and synchronise with the LHC beam collisions is described. The timing is found to be stable over a period of one year of operation at the nanosecond level. The normalisation of the gain of the system has also been described and this calibration is performed approximately every six months. The digitised data are processed by a series of FPGA algorithms that have been described and perform pedestal subtraction, common mode suppression and clusterisation. Errors in the system are also identified in the FPGA algorithms. A novel technique is applied of emulating the algorithms in bit-perfect C code which is used in the main analysis framework of the experiment to tune the operational parameters. A parameter retuning is required approximately every two months to ensure optimal performance. Single event upsets are observed in the front-end electronics at a rate of around 2.9 register bit-flips for all front-end ASICs combined per  $\text{pb}^{-1}$  of delivered integrated luminosity. Extensive data quality monitoring has been put in place, including automatic processing of each run, the use of a graphical user interface to display plots, and templated reports in an electronic logbook.

The sensors initially had a signal to noise ratio of approximately 20:1, with the noise depending on the strip capacitance. The hit resolution varies with pitch and track angle; for the optimal track angle of  $7\text{--}11^\circ$  it varies from 4  $\mu\text{m}$  in the 40  $\mu\text{m}$  pitch region to 20  $\mu\text{m}$  at 100  $\mu\text{m}$  pitch. This resolution has been achieved using analogue readout for the front-end ASICs and pulse-height weighted cluster position determination. The typical cluster occupancy in the experiment during 2011 operation was around 0.48% for randomly triggered events in beam-crossings, but rises to 0.93% for events that have passed the high level trigger. Faulty strips in the detector have been determined using noise distributions, occupancy spectra and the cluster finding efficiency. The detector has less than 1% of faulty strips. Tracks arising from interactions between the LHC beams and gas molecules are observed and provide a useful sample for alignment and for beam imaging for luminosity studies. Beam backgrounds giving rise to splashes of hits in localised regions of the detector are also seen. The radiation damage in the detector has been studied through the analysis of the currents drawn and charge collection versus voltage. Dedicated beam time is used for the latter study for which an automated procedure has been developed. The inner radius regions of the  $n^+$ -on- $n$  sensors are observed to have undergone space-charge sign inversion, which is expected due to their proximity to the LHC beams. Charge loss is also

observed to have developed after irradiation due to the presence of the second metal layer that is used for routing out the signals from strips on the sensor.

The track finding efficiency of the VELO has been determined using a tag and probe method using  $J/\psi$  decays, and is typically above 98%. The modules have been aligned using a track-based software alignment procedure. The position to which the VELO is inserted in each fill is measured by mechanical motion sensors and this is used to update the alignment. An alignment precision of  $1\ \mu\text{m}$  for translations in the plane transverse to the beam, and a  $5\ \mu\text{m}$  stability of the relative alignment of the two VELO halves over an operational year is obtained.

The LHCb physics selection and analysis of long-lived heavy flavour decays relies on the background rejection and flavour tagging from the impact parameters and vertexing performance of the detector. The vertex resolution is strongly dependent on the number of tracks in the vertex. A resolution of  $13\ \mu\text{m}$  in the transverse plane and  $71\ \mu\text{m}$  along the beam axis is achieved for vertices with 25 tracks. A 1D impact parameter resolution of  $12\ \mu\text{m}$  in the plane transverse to the beam for high momentum tracks is obtained. It is primarily determined by the detector cluster position resolution and the distance of the sensors for the LHC beams. For lower momentum tracks the impact of multiple scattering in the detector material becomes dominant, and an impact parameter resolution of  $35\ \mu\text{m}$  is achieved for particles with transverse momentum of  $1\ \text{GeV}/c$ . A decay time resolution of approximately 50 fs is obtained (evaluated for the  $B_s^0 \rightarrow J/\psi \phi$  decay channel) which plays a key role in many LHCb physics results.

## 7 Acknowledgements

This complex detector could only be constructed with the dedicated effort of many technical collaborators in the institutes forming the LHCb VELO Collaboration. A special acknowledgement goes to all our LHCb collaborators who over the years have contributed to obtain the results presented in this paper. We express our gratitude to our colleagues in the CERN accelerator departments for the excellent performance of the LHC. We thank the technical and administrative staff at the LHCb institutes. We acknowledge support from CERN and from the national agencies: CAPES, CNPq, FAPERJ and FINEP (Brazil); NSFC (China); CNRS/IN2P3 and Region Auvergne (France); BMBF, DFG, HGF and MPG (Germany); SFI (Ireland); INFN (Italy); FOM and NWO (The Netherlands); SCSR (Poland); MEN/IFA (Romania); MinES, Rosatom, RFBR and NRC “Kurchatov Institute” (Russia); MinECo, XuntaGal and GENCAT (Spain); SNSF and SER (Switzerland); NAS Ukraine (Ukraine); STFC (United Kingdom); NSF (USA). We also acknowledge the support received from the ERC under FP7. The Tier1 computing centres are supported by IN2P3 (France), KIT and BMBF (Germany), INFN (Italy), NWO and SURF (The Netherlands), PIC (Spain), GridPP (United Kingdom). We are indebted to the communities behind the multiple open source software packages we depend on. We are also thankful for the computing resources and the access to software R&D tools provided by Yandex LLC (Russia).

## References

- [1] LHCb Collaboration, A. A. Alves Jr. *et al.*, *The LHCb detector at the LHC*, JINST **3** (2008) S08005.
- [2] LHCb Collaboration, *LHCb VELO (VERtex LOcator) Technical Design Report*, LHCb-TDR-5, CERN-LHCC-2001-011.
- [3] LHCb Collaboration, R. Aaij *et al.*, *Measurement of  $\sigma(pp \rightarrow b\bar{b}X)$  at  $\sqrt{s} = 7$  TeV in the forward region*, Phys. Lett. **B694** (2010) 209, arXiv:1009.2731.
- [4] T. Sjostrand, S. Mrenna, and P. Z. Skands, *PYTHIA 6.4 physics and manual*, JHEP **0605** (2006) 026, arXiv:hep-ph/0603175.
- [5] R. Aaij *et al.*, *The LHCb trigger and its performance in 2011*, JINST **8** (2013) P04022, arXiv:1211.3055.
- [6] LHCb Collaboration, R. Aaij *et al.*, *Measurements of the branching fractions for  $B_{(s)} \rightarrow D_{(s)}\pi\pi\pi$  and  $\Lambda_b^0 \rightarrow \Lambda_c^+\pi\pi\pi$* , Phys. Rev. **D84** (2011) 092001, arXiv:1109.6831.
- [7] LHCb Collaboration, R. Aaij *et al.*, *Precision measurement of the  $B_s^0 - \bar{B}_s^0$  oscillation frequency with the decay  $B_s^0 \rightarrow D_s^-\pi^+$* , New J. Phys. **15** (2013) 053021, arXiv:1304.4741.
- [8] LHCb Collaboration, R. Aaij *et al.*, *Measurement of the CP-violating phase  $\phi_s$  in the decay  $B_s^0 \rightarrow J/\psi\phi$* , Phys. Rev. Lett. **108** (2012) 101803, arXiv:1112.3183.
- [9] M. Agari *et al.*, *Beetle – a radiation hard readout chip for the LHCb experiment*, Nucl. Instrum. Meth. **A518** (2004) 468.
- [10] G. Haefeli *et al.*, *The LHCb DAQ interface board TELL1*, Nucl. Instrum. Meth. **A560** (2006) 494.
- [11] A. Bates *et al.*, *LHCb vertex locator module characterisation and long term quality assurance tests*, Nucl. Instrum. Meth. **A611** (2009) 41.
- [12] A. Papadelis, *Characterisation and commissioning of the LHCb VELO detector*, PhD thesis, Vrije Universiteit, Amsterdam, June, 2009, CERN-THESIS-2009-044.
- [13] C. Parkes, S. Borghi *et al.*, *First LHC beam induced tracks reconstructed in the LHCb VELO*, Nucl. Instrum. Meth. **A604** (2009) 1.
- [14] S. Borghi, *LHCb vertex locator commissioning and results from the first LHC beam reconstructed tracks*, Nucl. Instrum. Meth. **A623** (2010) 156.
- [15] M. Clemencic, N. Gilardi, and J. Palacios, *LHCb conditions database*, LHCb-2006-017.

- [16] M. van Beuzekom, A. Van Lysebetten, and B. Verlaat, *CO<sub>2</sub> cooling experience (LHCb)*, LHCb-PROC-2007-025.
- [17] C. Ilgner *et al.*, *The Beam Conditions Monitor of the LHCb Experiment*, arXiv:1001.2487.
- [18] GEANT4, S. Agostinelli *et al.*, *GEANT4: a simulation toolkit*, Nucl. Instrum. Meth. **A506** (2003) 250.
- [19] LHCb, Collaboration, *LHCb VELO Upgrade Technical Design Report*, LHCb-TDR-13, CERN-LHCC-2013-021.
- [20] M. Ferro-Luzzi, T. Latham, and C. Wallace, *Determination of the aperture of the LHCb VELO RF foil*, LHCb-PUB-2014-012.
- [21] A. Bay *et al.*, *The LHCb VELO analogue transmission line*, Nucl. Instrum. Meth. **A614** (2010) 34.
- [22] T. Szumlak and C. Parkes, *Description of the Vetra Project and its Application for the VELO Detector*, LHCb-2008-022. CERN-LHCb-2008-022.
- [23] H. Bichsel, *Straggling in thin silicon detectors*, Rev. Mod. Phys. **60** (1988) 663.
- [24] R. Fruhwirth, *Application of Kalman filtering to track and vertex fitting*, Nucl. Instrum. Meth. **A262** (1987) 444.
- [25] W. Hulsbergen, *The global covariance matrix of tracks fitted with a Kalman filter and an application in detector alignment*, Nucl. Instrum. Meth. **A600** (2009) 471, arXiv:0810.2241.
- [26] S. D. B. Goddard, *Proceedings of the 2012 Evian Workshop on LHC Beam Operation*, CERN-ATS-2013-045.
- [27] R. B. Appleby *et al.*, *Simulation of machine induced background in the LHCb experiment: methodology and implementation*, IEEE Trans. Nucl. Sci. **59** (2012) 1681.
- [28] LHCb Collaboration, R. Aaij *et al.*, *Absolute luminosity measurements with the LHCb detector at the LHC*, JINST **7** (2012) P01010, arXiv:1110.2866.
- [29] C. Barschel, *Precision luminosity measurement at LHCb with beam-gas imaging*, PhD thesis, RWTH Aachen University, March, 2014, CERN-THESIS-2013-301.
- [30] A. Affolder *et al.*, *Radiation damage in the LHCb vertex locator*, JINST **8** (2013) P08002, arXiv:1302.5259.
- [31] A. Gureja *et al.*, *Use of IV (current vs voltage) scans to track radiation damage in the LHCb VELO*, LHCb-PUB-2011-020.

- [32] A. Hickling *et al.*, *Use of IT (current vs temperature) scans to study radiation damage in the LHCb VELO*, LHCb-PUB-2011-021.
- [33] M. Moll, *Radiation damage in silicon particle detectors*, PhD thesis, University of Hamburg, 1999, DESY-THESIS-1999-040.
- [34] S. Viret, C. Parkes, and M. Gersabeck, *Alignment procedure of the LHCb vertex detector*, Nucl. Instrum. Meth. **A596** (2008) 157, [arXiv:0807.5067](#).
- [35] M. Gersabeck, S. Viret, C. Parkes *et al.*, *Performance of the LHCb vertex detector alignment algorithm determined with beam test data*, Nucl. Instrum. Meth. **A596** (2008) 164, [arXiv:0807.5069](#).
- [36] V. Blobel and C. Kleinwort, *A new method for the high precision alignment of track detectors*, [arXiv:hep-ex/0208021](#).
- [37] M. Pivk and F. R. Le Diberder, *sPlot: a statistical tool to unfold data distributions*, Nucl. Instrum. Meth. **A555** (2005) 356, [arXiv:physics/0402083](#).